Determination of plasma-ion velocity distribution via charge-exchange recombination spectroscopy

R. J. Fonck, D. S. Darrow, and K. P. Jaehnig
Plasma Physics Laboratory, Princeton University, Princeton, New Jersey 08544
(Received 21 November 1983)

Spectroscopy of line radiation from plasma impurity ions excited by charge-exchange recombination reactions with energetic neutral-beam atoms is rapidly becoming recognized as a powerful diagnostic for magnetically confined tokamak plasmas. Ion temperature, bulk plasma motion, impurity transport, and more exotic phenomena such as fast alpha-particle distributions can all be measured with this technique. In particular, it offers the capability of obtaining space- and time-resolved ion temperature and toroidal plasma rotation profiles with relatively simple optical systems. Cascade-corrected excitation rate coefficients for use in both fully stripped impurity density studies and ion-temperature measurements have been calculated for the principal $\Delta n = 1$ transitions of He^+, C^{5+}, and O^{7+} with neutral-beam energies of 5—100 keV/amu. Line intensities and profiles can be affected by atomic fine structure, l-mixing collisions, motional Stark effects, and product ions created in the neutral-beam region which drift into the viewing sightline. General estimates of the importance of these effects for the transitions of interest are provided, along with specific examples calculated for the PDX (Poloidal Divertor Experiment) and TFTR (Tokamak Fusion Test Reactor) tokamaks. A fiber optically coupled spectrometer system has been used on PDX to measure visible He^+ radiation excited by charge exchange to illustrate some of these points. Central ion temperatures up to 2.4 keV and toroidal rotation speeds up to 1.5×10^7 cm/s were observed.

I. INTRODUCTION

The determination of ion velocity distributions in high-temperature plasmas is of fundamental importance in controlled fusion research, and several techniques are presently used to measure these distributions to determine, among other quantities, the plasma ion temperature.[1] However, detailed time evolutions and radial profiles of ion temperatures have not been routinely available in magnetically confined plasma experiments in spite of their relevance to understanding the confinement properties of particular configurations. This is in contrast to our knowledge of other basic plasma properties such as electron density and temperature, for which radially resolved profiles are often the *sine qua non* of a reasonable description of the plasma. In addition, given the difficulty in diagnosing hot plasmas, it traditionally has been desirable to make redundant measurements of basic parameters. This is especially true as plasma experiments become larger and more expensive, with correspondingly fewer plasma shots available.

The study of the profiles of spectral lines emitted from hot plasmas has been a time-honored means of obtaining the ion velocity distribution. The Doppler broadened width of the line profile gives a measure of the bulk thermal temperature of the emitting ions if broadening due to mass motion turbulence is negligible,[2] and the shift of a line center gives a measure of the plasma bulk motion, such as may arise in a rotating plasma in a toroidal confinement device.[3] Detailed line-shape studies may reveal more exotic information such as the distribution of fast alpha particles in a near-ignition plasma or the presence of nonthermal tails generated by rf heating.[4] Obviously, any of the above measurements presuppose the existence of radiating ions in the hot plasma core whose spatial distributions are limited and known in a given experiment. Given that such ions exist and can be spatially localized, a detailed knowledge of line excitation mechanisms is then necessary in order to recognize possible distortions of the line profile. These effects may then be compensated for, or preferably such knowledge may allow one to choose appropriate transitions and ions so as to minimize such distortions.

In this paper, we discuss a relatively new approach to ion velocity distribution measurements in hot plasmas which uses the active spectroscopic technique of charge-exchange recombination spectroscopy (CXRS).[5] This approach holds promise for providing a relatively simple measurement of ion temperatures with good spatial localization in fusion grade plasmas, and straightforwardly allows time-resolved ion temperature profiles in a single plasma shot. Ion temperature and toroidal rotation velocity profiles obtained on the Poloidal Divertor Experiment (PDX) tokamak using CXRS are given as an example of such measurements. Several considerations which affect the validity of CXRS measurements of ion velocity distributions are also addressed.

The application of CXRS to the diagnosis of high-temperature plasmas has received much attention in recent years and the rapid maturation of this technique indicates its usefulness. Fonck, Goldston, Kaita, and Post,[5] using results from the PDX tokamak, and Isler and Murray[6] with data from ISX-*B* (Impurity Study Experiment) originally discussed the measurements of ion temperature and plasma rotation using CXRS. The basic technique consists of measuring spectral profiles and shifts of emis-

sion lines from ions in the plasma which are excited by charge-exchange recombination reactions. Typically, a fully ionized low-Z impurity ion and fast neutral atoms (typically H^0 or D^0) from either a diagnostic neutral beam or a heating neutral beam are used. The recombination process

$$H^0 + A^{Z+} \rightarrow H^+ + A^{(Z-1)+}(n,l) \quad (1)$$

leaves the resulting ion in an excited state (n,l) which subsequently decays through photon emission. For common low-Z hydrogenic ions such as He^+, C^{5+}, and O^{7+}, these spectral lines have wavelengths which range from the extreme ultraviolet to the visible spectral regions. The cross sections for such processes are often large ($\gtrsim 10^{-16}$ cm^2) and hence measurable intensities are obtained with moderate neutral densities.

Local impurity ion densities and transport properties of fully stripped low-Z impurities have been studied via reaction equation (1) using the heating neutral beams in the ORMAK (Oak Ridge Tokamak) (Ref. 7) and ISX-B (Ref. 8) tokamaks, and using diagnostic neutral beams in the T-10 (Ref. 9) and PDX (Ref. 10) tokamaks. The use of reaction equation (1) for the diagnosis of alpha particles has also been discussed.[4,11] In addition to hydrogen neutral beams, lithium beams are currently in use to study partially ionized charge states of impurities at the plasma edge.[12] In general, fully ionized low-Z impurities are most useful for ion temperature and plasma rotation measurements because naturally occurring impurities such as C and O are fully stripped at tokamak electron temperatures and thus do not strongly radiate and perturb the plasma. In addition, these ions are sufficiently abundant at all radii in the plasma due to cross field transport[10] that no additional contamination of the plasma with impurity atoms is necessary and a full radial profile can be obtained by observing a single spectral line. Measurements of central ion temperature and/or plasma rotation using CXRS have most recently been reported from the PDX,[13] ISX-B,[14] Doublet-III,[15] and DITE (Divertor Injection Tokamak Experiment) (Ref. 16) tokamak groups.

In addition to the CXRS approach described above, several other methods of determining ion velocity distributions in tokamaks presently are available,[1,2] but all of these have limitations. The most common measurement is to energy analyze the fast neutrals produced in the center of the plasma by charge exchange with background neutral atoms. This technique measures only the high-energy tail of the ion distribution which can escape from the plasma center without reionization and it is subject to uncertainties due to ion-orbit effects and non-Maxwellian distributions. As tokamak plasmas become denser, they become increasingly opaque to the central charge-exchange-produced neutrals and the density of background neutrals decrease. Both of these effects result in a reduction of the fast neutral flux escaping from the plasma core region. Thus a diagnostic neutral beam is necessary to raise locally the central neutral density to give sufficient signal levels and provide good spatial resolution. T_i may also be determined from analysis of thermonuclear neutron emission, but this again is sensitive primarily to the high-energy tail of the ion velocity distribution, and spatial resolution is not yet possible. The calculation of T_i from neutron emission also presupposes knowledge of the plasma ionic composition. Measurements of the Doppler broadening of impurity line emissions from partially ionized atoms excited by electron impact give measures of the bulk impurity ion energy distribution which can usually be related to the plasma ion temperature quite reliably. The wavelengths of interest for such measurements can lie in the x-ray, extreme ultraviolet, or near-ultraviolet spectral regions. If supplementary information on the ion species radial distribution is available (which is not always the case), line profile measurements from several impurity charge states can provide radially resolved $T_i(r,t)$ measurements. However, it is obviously necessary that a sufficient number of highly ionized heavy atoms which are not fully stripped be present in the hot plasma core, which has $kT_e \simeq 1$—5 keV typically. The requirement for a density sufficiently high to give an adequate signal level may conflict with the need to minimize the heavy impurity concentration. As central electron temperatures increase in the next generation of tokamaks, such as TFTR (Tokamak Fusion Test Reactor) and JET (Joint European Torus), so likewise will the atomic number Z necessary to assure incomplete ionization in the plasma core. The decoupling of impurity ion temperature from the bulk plasma ion temperature must also be considered carefully as Z increases.

The CXRS measurements of ion velocity distributions are less subject to the limitations mentioned above and will be useful on both the present and next generation of confinement machines with large, hot, dense plasmas. Like other Doppler broadening measurements, the bulk ion temperature is measured. Since low-Z impurities can be used, no heavy impurity injection is necessary, thus reducing the possibility of perturbing the plasma by significantly increasing the impurity content. Furthermore, use of light impurities ensures the measurements will closely reflect the temperature of the bulk plasma. Naturally occurring concentrations ($N_Z/N_e \sim 1\%$) of C and O are quite sufficient for such measurements, and as mentioned earlier, a single spectral line from a single ion species can provide a full radial profile of T_i since cross-field transport is usually sufficient to ensure fully stripped C and O throughout the plasma. Since the heating neutral beams can often be used for these measurements, the CXRS technique is nonperturbing. Good spatial resolution is obtained by viewing across a collimated neutral beam with a collimated spectrometer, and the radial profile is produced by simply changing the viewing direction of the spectrometer. Thus the measurement is similar to a crossed-beam technique and neither prior knowledge of impurity radial distributions nor Abel inversions are necessary. It has only the relatively minor requirement that optical access to view the beam must be available. Judicious choices of beam injection angle and/or spectrometer viewing direction allow spatially resolved measurements of plasma rotation in any direction of interest (e.g., toroidal or poloidal directions in toroidal confinement devices).

A significant advantage of using CXRS to determine ion velocity distributions is the fact that several of the

spectral lines excited by charge exchange have relatively long wavelengths, ranging all the way to the visible spectral range for spectrally isolated $\Delta n = 1$ transitions between Rydberg states of He^+ (e.g., $\Delta n = 4$-3 at 4686 Å), C^{5+} (8-7 at 5290 Å), and O^{7+} (10-9 at 6070 Å). These lines are particularly interesting because they allow ion temperature measurements while requiring only radiation-hardened fiber optic access to the reactor vessel. The detectors and spectrometers can be remotely located and shielded. Indeed, initial efforts on PDX and Doublet-III concentrated on He II 4686 Å due to easy visible wavelength access to the tokamak via fiber optics. Even when the visible lines are not sufficiently bright for line profile measurements (a discussion of line intensities follows in Sec. II), sufficiently intense lines will usually lie at $\lambda \geq 1000$ Å and no grazing incidence optics or vacuum access are required. Since typical tokamak plasmas of interest have $kT_i \geq 0.5$ keV and the ion mass is low, linewidths produced by thermal Doppler broadening are readily resolved with conventional spectroscopic instrumentation.

The use of CXRS to measure ion velocity distributions does, of course have some limitations and constraints. Fine-structure effects and product ion background effects will be discussed in detail in later sections. An obvious requirement is that good beam-spectrometer geometry is needed, and, especially with tangential beam injection in toroidal devices, not all radii may be accessible. When several beams intersect the spectrometer line of sight, modulation of a single beam is necessary to obtain good spatial localization. On plasma devices with only rf heating, a diagnostic neutral beam would be necessary. It should be noted that spectral lines chosen for optimal ion temperature measurements are usually not attractive for absolute impurity density measurements, so another spectrometer would probably be needed for such measurements. Finally, if good absolute intensity results are desired, accurate cross sections and beam particle densities must be calculated for each case of interest.

In this paper, we expand upon our earlier work[5] by discussing a variety of effects that can affect the applicability of CXRS to ion velocity distribution measurements. The emphasis is on estimating these effects to determine when the measurements are valid rather than presenting complete theoretical discussions. For example, a fully rigorous atomic line-structure calculation is not performed but estimates are used to evaluate its importance. As an example of the application of this diagnostic technique, we also present the first radial profiles of T_i and toroidal rotation velocity obtained via CXRS on the PDX tokamak.

The next section discusses the expected line intensities for most $\Delta n = 1$ transitions of interest for He^+, C^{5+}, and O^{7+}. The trade-offs between the desire for long wavelengths and high intensities are indicated. Some level-mixing effects which may significantly alter the expected line intensities are also considered. Section III contains a discussion of the influence of atomic fine structure on the determination of bulk ion temperature. Section IV considers the radial delocalization of the observed emissions due to recombined ions drifting into the spectrometer line of sight. This effect is most important in the case of He^+, and specific examples for PDX and TFTR are calculated as illustrations. Finally, Sec. V presents results of measurements of ion temperature and toroidal rotation velocity radial profiles using CXRS with He II 4686-Å radiation.

We concentrate on discussions of $\Delta n = 1$ transitions in C and O because these transitions have the longest wavelengths and these elements are typically the most abundant impurities in magnetic confinement devices. In addition, He is discussed both because of its long wavelength transitions and its relevance to helium ash measurements. The concentration on low-Z impurities instead of the plasma ions themselves (H^+ or D^+) arises from the fact that, in most experiments, there can be an unknown mixture of H^+ and D^+ depending on the particular running conditions. However, when the plasma working gas does contain only one isotopic species, this technique can be used on the plasma ions themselves.[16] The work presented here can obviously be extended to other low- and high-Z impurities (e.g., Ti or Fe), even to the hard-to-detect He-like and H-like charge states of heavy metals (e.g., Fe^{24+}). Finally, we note that a tokamak plasma device will be assumed in all further discussions, but the diagnostic approach would be similar in other magnetically confined plasma experiments.

II. LINE INTENSITIES

The ability to calculate spectral line intensities for CXRS measurements is necessary in order to evaluate which lines to use for specific purposes. While the determination of the density of a fully stripped impurity via CXRS obviously requires knowledge of the total excitation rate for the line measured,[8–10] it is also important to estimate excitation rates for other lines which may be more suitable for ion velocity measurements (e.g., high-n transitions at long wavelengths) than for impurity density measurements. Estimates of excitation rate coefficients also allow us to determine which line intensities will be dominated by charge exchange rather than electron impact excitation, and hence allow good spatial localization of the emitting source. In this section we discuss excitation rates applicable to CXRS and processes which may alter these rates, especially for long-wavelength emissions arising from Rydberg state transitions.

When a spectrometer sightline crosses a neutral beam, the intensity for a transition at wavelength λ due to prompt charge-exchange (cx) recombination events is given by

$$B_\lambda^{cx} = \frac{1}{4\pi} \sum_{j=1}^{M} \langle \sigma v \rangle_j^\lambda \int N_Z N_j dl \ , \tag{2}$$

where $\langle \sigma v \rangle_j^\lambda$ is the rate coefficient for excitation of wavelength λ by the jth beam velocity component, N_Z is the impurity ion density, and N_j is the beam particle component at velocity $v_j = v_1/\sqrt{j}$. The summation is over the various beam energy components, and usually $M = 3$ for hydrogen beams. The intensity contribution from the relatively slow halo neutrals is negligible for most of the considerations in this paper and hence neglected. The in-

tegral in Eq. (2) is along the spectrometer line of sight and is replaced by $N_Z N_j l_j$ if the intersection length for the sightline and beam is small. Here, l_j denotes the effective path length of the spectrometer line of sight through the beam for the jth beam component. If $\langle \sigma v \rangle_j^{\lambda}$ is in units of $\mathrm{cm}^3\,\mathrm{s}^{-1}$, and N_Z and N_j in units of cm^{-3}, $B_{\lambda}^{\mathrm{cx}}$ has the usual intensity units of photons/cm^2 s sr.

It is worth noting as an aside that $B_{\lambda}^{\mathrm{cx}}$ in general does not depend on the electron temperature, and one can expect to observe ions in regions of the plasma where T_e is too low to excite the transitions via electron collisions (i.e., near the plasma edge). This also eases the uncertainties in calculating local impurity densities N_Z.

The problem of calculating $B_{\lambda}^{\mathrm{cx}}$ consists of calculating $N_j l_j$ and $\langle \sigma v \rangle_j^{\lambda}$ for specific cases. The beam particle column densities are readily calculated via a beam attenuation code, given specific plasma density and temperature profiles and a specific beam-spectrometer geometry. These calculations use the total stopping cross sections used in Ref. 17 and are not discussed further here except as the results are applied to specific cases of interest.

Several theoretical techniques are used to calculate the cross section $\sigma(n,l)$ for populating a given atomic level with principal quantum number n and orbital angular momentum number l after a charge-exchange collision, with different techniques appropriate for different energy ranges.[18] The calculation of specific values of $\sigma(n,l)$ for given energy ranges is presently a very active area of theoretical atomic physics, and values for a wide range of beam energies are becoming available. Only some of this work will be referenced in this paper as it is needed. A few general features of these results are worth noting however. The charge-exchange reaction tends to be a resonant process in that the electron from the neutral beam particle prefers to transfer to excited levels in the product ion [A^{Z-1} in Eq. (1)] which preserve its orbital energy and radius.[19] This leads to a peaking of $\sigma(n) = \sum_l \sigma(n,l)$ in n with $n_{\max} \approx Z^{3/4}$. As the beam energy increases, the width of this distribution in n increases and higher n states are populated. The l distribution of $\sigma(n,l)$ for a given n state also is peaked, with $\sigma(n,l)$ increasing sharply as l increases for $n \lesssim n_{\max}$ and tending to level off or peak at $l \sim n_{\max}$ for $n > n_{\max}$. Thus, for transitions between states near or below $n_{\max}$, the high-l (yrast) states are predominantly populated and the subsequent $\Delta n = 1$ decay transitions are the most intense. The change-exchange reaction produces very little momentum charge for the recombined ion and hence does not disturb the ion velocity distribution.

The observed intensities are determined by the cascade of the excited electrons from their initial distribution produced by the charge-exchange reaction, and this of course results in a line-intensity pattern that does not at first glance look like the initial $\sigma(n,l)$ distribution given by theory. For example, Fig. 1(a) shows schematically the distribution of $\sigma(n,l)$ for a given case of $H^0 + C^{6+} \rightarrow H^+ + C^{5+}(n,l)$ as calculated by Green, Shipsey, and Browne.[20] The cascade-corrected cross section for the (n,l) level is given by

$$\sigma_c(n,l) = \sum_{k=1}^{\infty} \sum_{l_k=0}^{n+k-1} [b_{n,l;n+1,l_1} b_{n+1,l_1;n+2,l_2} \times \cdots \times b_{n+k-1,l_{k-1};n+k,l_k} \sigma_d(n+k,l_k)] , \tag{3}$$

where $\sigma_d(n,l)$ is the direct charge-exchange cross section and $b_{nl;n'l'}$ is the branching ratio for electric dipole transitions from level $n'l'$ to nl (note that $b_{nl;n'l'} = 0$ unless $l' = l \pm 1$). These branching ratios for hydrogenic atoms are readily calculated using standard references. The sum in Eq. (3) is terminated at some large value of n (usually taken to be 10 herein) beyond which σ_d is negligible. The cascade-corrected cross sections for the case in Fig. 1(a)

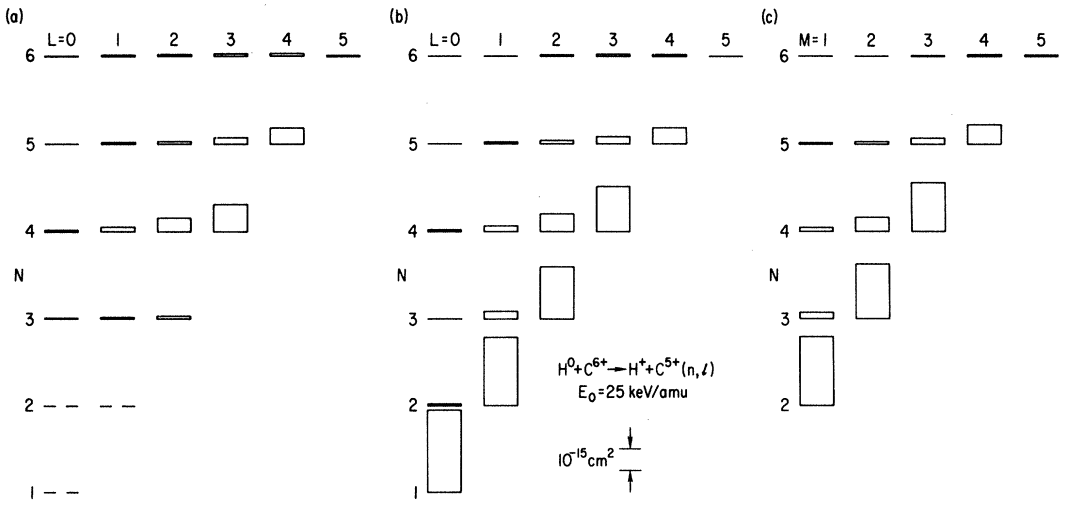

FIG. 1. Schematic of cross sections of interest for $H^0 + C^{6+} \rightarrow H^+ + C^{5+}(n,l)$ at 25 keV/amu with the direct charge-exchange cross sections taken from Ref. 18. (a) Cross section for populating each level (n,l) directly via charge exchange; (b) cascade-corrected total cross sections for populating each (n,l) level; (c) total effective cross section for excitation of an $n \rightarrow m$ transition.

are shown in Fig. 1(b). Since atomic fine structure usually is not resolved, we are interested in the total effective cross section for excitation of a given $n' \rightarrow n$ transition which is given by summing over all the l levels with the appropriate branching ratios. These cross sections are given by

$$\sigma(n,n') \equiv \sigma^{\lambda} = \sum_{l=0}^{n'-1} \sigma(n',l) b_{nl,n'l'} \tag{4}$$

with $l = l' \pm 1$. Figure 1(c) shows these resultant total cross sections for line excitation for the case of Fig. 1(a). The transitions between lowest n states will be brightest and will have intensities which are least sensitive to the original $\sigma_d(n,l)$ distribution. These features make the short wavelength transitions between low n states most attractive for impurity density measurements since the $\langle \sigma v \rangle^{\lambda}$ rates can be reliably calculated.

Since these cascade calculations are somewhat tedious and the results are needed for several CXRS applications, we present in Figs. 2–6 total effective rate coefficients for excitation via charge exchange for the important $\Delta n = 1$ transitions of He II, C VI, and O VIII, using values of $\sigma_d(n,l)$ provided by several authors. The results of Green, Shipsey, and Browne[20,21] for $H^0 + C^{6+}$ and $H^0 + O^{8+}$ were obtained using the perturbed stationary state method including molecular states for the specific system of interest and are the most accurate for this energy range. The more general unified distorted-wave approximation (UDWA) calculations of Ryufuku and co-workers,[22,23] while not as exact (especially at low energies), provide $\sigma_d(n,l)$ over a very wide range of beam energy, Z, and n, and thus are most useful for global estimates of intensities. The curves drawn in Figs. 2–6 are our interpolations between the few points in energy for which the $\sigma_d(n,l)$'s are provided. The tendency for the long-wavelength higher-n transitions to be excited only at high beam energies is evident in these results, as is the tendency for cross sections to peak at values of $n_{\max} \sim Z^{3/4}$. For example, the excitation rate coefficient for transitions drop rapidly as n increases above $n = 2$ in He II, while the sharp drop in $\langle \sigma v \rangle^{\lambda}$ for C VI does not appear until $n \gtrsim 5$.

While the theoretical cross sections $\sigma_d(n,l)$ provide the populations of a given level via direct charge-exchange events, the cascade process can be significantly affected by the surrounding plasma environment. Several processes can cause transfer between different l levels before an electron drops to lower states via photon radiation. These l-mixing processes can cause a distortion of the relative populations among the excited levels in a given state (i.e., given n) and affect line intensities and fine-structure line profiles. Other effects, such as ionization of the ion from the excited states before photon emission, tend not to be as important for typical tokamak plasmas; we discuss only collisional l mixing and possible l mixing due to the motional Stark effect[24] produced by ion thermal motion in the magnetic field. As mentioned earlier, the emphasis here is on obtaining estimates as to when these l-mixing processes are important rather than providing a rigorous theoretical discussion of their details.

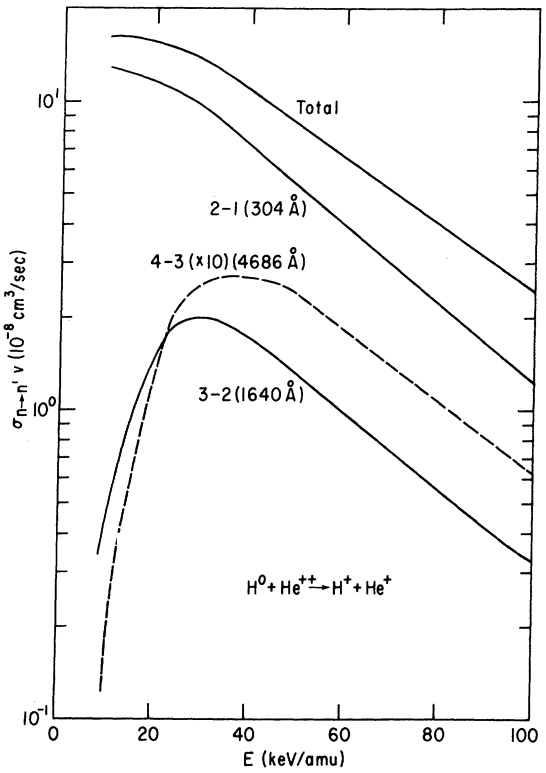

FIG. 2. Rate coefficients for excitation of principal $\Delta n = 1$ transitions in He^+ via charge-exchange recombination. Unified distorted-wave cross sections from Ref. 23 are used. The wavelength for each transition is given in parentheses.

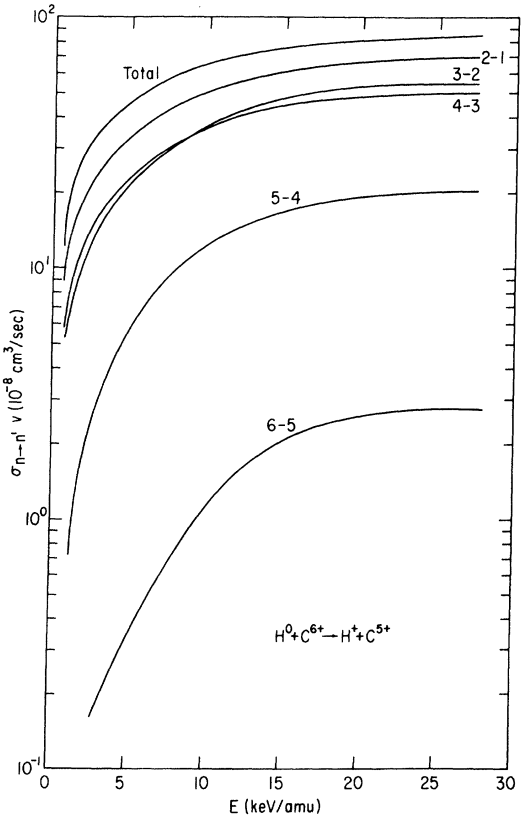

FIG. 3. Excitation rate coefficients for $\Delta n = 1$ transitions in C^{5+} using the perturbed stationary state cross sections from Ref. 20.

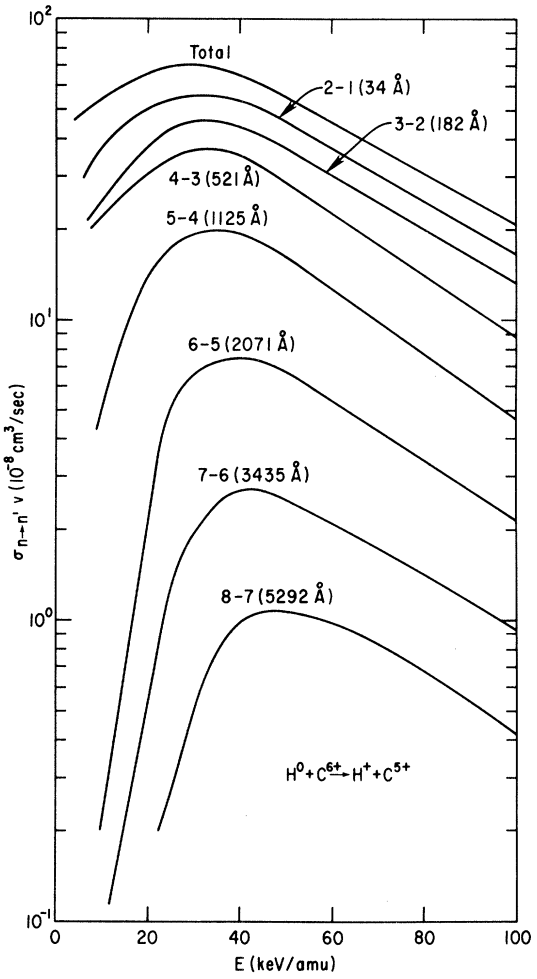

FIG. 4. Excitation rate coefficients for $\Delta n = 1$ transitions in C^{5+} using the unified distorted-wave cross sections from Ref. 23. The wavelength for each transition is given in parentheses.

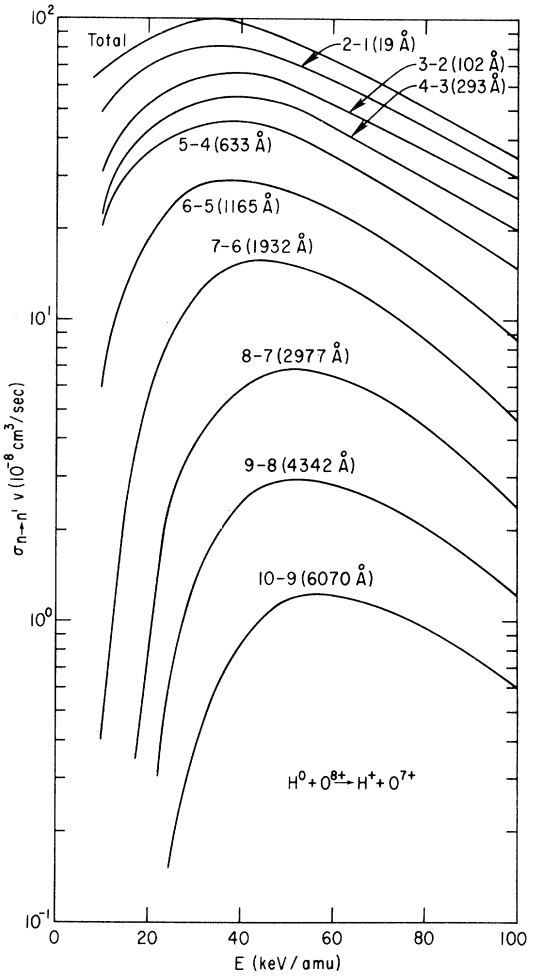

FIG. 6. Excitation rate coefficients for $\Delta n = 1$ transitions in O^{7+} using the UDWA cross sections of Ref. 23. The wavelength for each transition is given in parentheses.

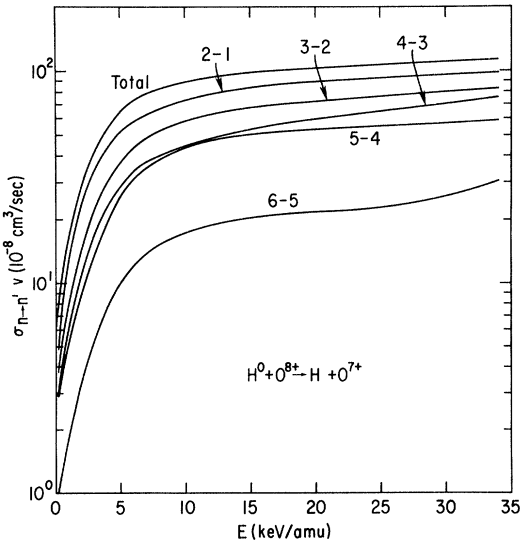

FIG. 5. Excitation rate coefficients for $\Delta n = 1$ transitions in O^{7+} using the perturbed stationary state cross sections from Ref. 21.

The l-mixing effects of ion-ion collisions have been discussed by Pengelly and Seaton[25] for planetary nebulae with $N_e \approx 10^4$ cm^{-3} and $kT_e \approx kT_i = 1$ eV, and we simply expand on their discussion to include a plasma regime typical of contemporary fusion experiments ($N_e \approx 10^{13}$–10^{14} cm^{-3}, $kT_i \approx 1$–10 keV). They use an impact parameter collision model with straight line trajectories to derive the net rate coefficients for transitions between nearly degenerate l states due to charged particle collisions. This model is not rigorously applicable to our case since it neglects the Coulomb repulsion between the ions, and more precise treatments have since become available.[26,27] However, its simple and general nature allows us to at least estimate whether these processes are important at all, and, if they are found to be so, this approach may motivate more detailed calculations in future work. We thus follow their discussion to extrapolate the results to our regime of interest. The rate coefficient for $n,l \rightarrow n,l'$ ($l' = l \pm 1$) transitions between nearly degenerate levels in hydrogenic ions with charge Z and due to collisions with ions of charge z is given by (in cm^3 s^{-1})

$$q_{nl}^{Z,z}=9.93\times10^{-6}\left[\frac{\mu}{m}\right]^{1/2}\frac{D_{nl}}{T_i^{1/2}}\left[11.54+\log_{10}\left[\frac{T_i m}{D_{nl}\mu}\right]+2\log_{10}\bar{R}_c\right], \tag{5}$$

where

$$D_{nl}=\left[\frac{z}{Z}\right]^2 6n^2(n^3-l^2-l-1), \tag{6}$$

μ is the reduced ion mass of the colliding particles, T_i is the ion temperature in K, and m is the electron mass. If the Debye radius is used as a cutoff length for the collisional interaction, the last term in Eq. (5) is given by

$$2\log_{10}\bar{R}_c\approx1.68+\log_{10}(T_i/N_e) \tag{7}$$

with N_e being the electron density in units of cm^{-3}.

Assuming $m_Z=2Zm_p$ and $m_z=2zm_p$ where m_p is the proton mass, we find that for z, $Z\lesssim10$, $n\leq20$, and $kT_i\leq10$ keV, within a variation of only $\pm26\%$,

$$q_{nl}^{Z,z}=q_{nl}^{H,H}\left[\frac{Zz}{Z+z}\right]^{1/2}\left[\frac{z}{Z}\right]^2\frac{0.091}{\sqrt{T_i}}, \tag{8}$$

where from now on T_i is in keV and $q_{nl}^{H,H}$ is the proton-proton l-mixing rate calculated by Pengelly and Seaton for $N_e\approx10^4$ cm^3 and $T\approx1$ eV. This form allows their numerical results for $q_{nl}^{H,H}$ to be scaled directly to the present cases of interest. If several ion species are present, the total reaction rate for l-mixing transitions from state (n,l) to $(n,l\pm1)$ is given by

$$\sum_z N_z q_{nl}^{Z,z}=q_{nl}^{H,H}\frac{0.091}{Z^2\sqrt{T_i}}\sum_z N_z z^2\left[\frac{Zz}{Z+z}\right]^{1/2}$$

$$\approx q_{nl}^{H,H}\frac{0.106}{\sqrt{T_i}}\frac{1}{Z^2}\sum_z N_z z^2, \tag{9}$$

where the square root term in the sum has been replaced by its median value assuming z and Z range from 1 to 10. For z and $Z\leq10$, $n\leq20$, and $T_i\leq10$ keV, the relation in Eq. (8) is accurate to $\pm68\%$. If heavy impurities have negligible densities, the sum in Eq. (9) is just the product N_eZ_{eff} where $Z_{\text{eff}}\equiv\sum N_z z^2/N_e$, and Eq. (9) reduces to

$$\sum_z N_z q_{nl}^{Z,z}=q_{nl}^{H,H}\frac{0.106}{\sqrt{T_i}}\frac{Z_{\text{eff}}}{Z^2}N_e\equiv(\tau_{nl}^Z)^{-1}. \tag{10}$$

The l levels can be considered to be mixed collisionally when $A_{nl}^Z\tau_{nl}^Z\gtrsim1$ where

$$A_{nl}^Z=Z^4A_{nl}^H \tag{11}$$

is the total spontaneous emission rate out of the (n,l) level. For complete l mixing of a given n state, a sum over all l values must be made, and the resulting critical value of N_e above which a particular n state will be mixed collisionally is given by

$$N_e(n)\frac{Z_{\text{eff}}}{Z^6}\frac{0.106}{\sqrt{T_i}}=\frac{1}{\tau_n^H q_n^H}. \tag{12}$$

This result shows that we can replace the critical N_e given by Pengelly and Seaton for a given n state by the quantity on the left side of Eq. (12) to estimate the n states which are mixed in our denser, hotter plasmas. This procedure eliminates the need to reproduce the laborious evaluations of excitation and spontaneous emission rates for each case. Since $\tau_{n,l}\sim n^3$ and $q_{n,l}\sim n^{3-4}$ [cf. Eq. (6)], the critical density for a given (n,l) sublevel varies roughly as n^{-6} and one expects this criterion for l mixing to be fairly sharp in n. Using the results from Fig. 4 of Pengelly and Seaton, which plots the critical density $N_{e,c}(n)$ as a function of n, we use Eq. (12) to produce Fig. 7, which plots the critical value of N_e (in units of 10^{13} cm^{-3}) as a function of n. If, for a given case, the value of the ordinate lies above the curve for a given n state, collisional l mixing can be neglected to lowest order, while a statistical distribution among l states can be assumed if the value falls below the curve. For example, with $N_e=2\times10^{13}$ cm^{-3}, $T_i=1$ keV, and $Z_{\text{eff}}=2$ (typical PDX parameters halfway out from the center), all levels with $n\gtrsim5$ for carbon and $n\gtrsim6$ for oxygen can be considered to be mixed collisionally, and the relative population among the various l levels in a given n state is then given by their statistical weights $(2l+1)/n^2$.

Before examining the consequences of this l mixing on the rate coefficients, we consider a second l-mixing process which can be dominant in certain parameter regimes. As an ion gyrates around a magnetic field line, it sees an electric field in its own frame which is perpendicular to the magnetic field direction and whose magnitude is given approximately by (in V/m)

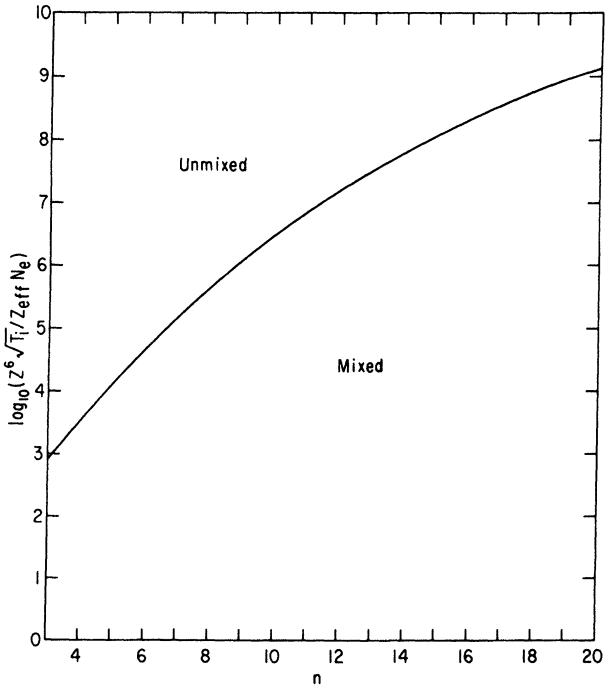

FIG. 7 Estimate of critical n value for onset of l mixing due to ion-ion collisions. T_i is in keV and N_e in units of 10^{13} cm^{-3}.

$$F_{\vec{v}\times\vec{B}} \simeq vB \simeq 2.20\times 10^5 \left[\frac{T_i}{Z}\right]^{1/2} B \ , \tag{13}$$

where the ion thermal speed is used and T_i is in keV and B in T. Clearly, large fields can be experienced and the atomic Stark effect acts to mix states of different parity (i.e., l). Since both Zeeman and Stark splitting of the various atomic sublevels are simultaneously present, the situation can become rather complex as n increases and the perturbations become comparable to the energy spacing between adjacent fine-structure levels. It is just this strong mixing regime which is of interest for gaining estimates for critical n levels above which this motional Stark effect can cause severe l mixing. The problem is not nearly as amenable to straightforward calculation as was the collisional l-mixing case, but a crude treatment does allow progress to be made. In the spirit of other qualitative treatments of strong field mixing regimes in atomic structure, we obtain an estimate for the onset of Stark mixing between different l levels by comparing the energy shift due to the motional Stark field to the field-free fine-structure energy differences.

Ignoring nuclear mass effects and Lamb shifts, the energy of a given level in a hydrogenic ion with nuclear charge Z, principal quantum number n, and total angular momentum j is given by[28]

$$E(n,j) = -\frac{Z^2}{n^2}\left[1+\frac{(\alpha Z)^2}{n}\left[\frac{1}{k}-\frac{3}{4n}\right]\right]\mathscr{R} \ , \tag{14}$$

where $\mathscr{R}$ is the Rydberg energy (13.6 eV), α is the fine-structure constant, and $k = j+\frac{1}{2} = 1,2,\ldots,n$. Then the energy splitting between fine-structure levels in the same n level with j values differing by 1 is

$$\Delta E_{\rm FS} = -\frac{\alpha^2 Z^4}{n^3}\frac{1}{k(k+1)}\mathscr{R} \ . \tag{15}$$

In the limit where the Stark shifts are much larger than the fine-structure separation, the n manifold splits into a series of equally spaced levels which have a total energy separation of[29]

$$\Delta E_S \simeq 3F\frac{4\pi\epsilon_0 a_0}{e^2}\frac{n(n-1)}{Z}\mathscr{R} \ , \tag{16}$$

where F is the applied electric field and a_0 is the Bohr radius. Of course, severe l mixing occurs long before this Stark pattern fully develops. We estimate when l mixing will start by solving for the n value at which the fine-structure separation is equal to the energy shift of the electron due to the motional electric field.

As T_i or B increases, the motional Stark effect first arises as a second-order perturbation in the energy of magnetic sublevels of a given j manifold.[30] This occurs because the electric field is perpendicular to the magnetic field and couples states through the $\langle njm \mid x \mid njm'\rangle$ matrix elements with the selection rule $m' = m\pm 1$ (or $m_{l'} = m_l \pm 1$) assuming the B field is along the Z axis. But these m levels are no longer degenerate due to the presence of the magnetic field, and one thus returns to a quadratic Stark effect instead of the usual hydrogenic linear Stark effect. That is, the atom in the magnetic field has no electric dipole moment perpendicular to the field even though, in the absence of the magnetic field, the j degeneracy of the energy levels allows a net dipole moment to exist.

The resulting second-order shift due to the motional Stark field is given by

$$\Delta E^Q = \frac{|\langle njm \mid exF_{\vec{v}\times\vec{B}} \mid njm'\rangle|^2}{2\mu_0 B}$$

$$\approx (eF_{\vec{v}\times\vec{B}})^2 \frac{n^4}{Z^2}\frac{a_0^2}{\mu_0 B} \ , \tag{17}$$

where we have approximated the matrix element of x by the size of the Bohr radius for the nth excited state. In Eq. (17), μ_0 is the Bohr magneton. Equating ΔE^Q with the spacing between the most closely spaced field-free fine-structure levels yields a rough estimate of the minimal value of n for the onset of l mixing. Combining Eq. (15) (with $k=n$) and Eq. (17), we get for $n \gg 1$

$$n_S^Q = 2.04\left[\frac{Z^7}{T_i B}\right]^{1/9} \ , \tag{18}$$

with T_i in keV and B in T. Stark mixing of l levels can be considered important for all $n \gtrsim n_S^Q$. This estimate is, of course, crude and somewhat pessimistic since we only require that the Stark shift equal the minimal fine-structure spacing, but it does illustrate the general features that n_S depends almost linearly on Z and very weakly on T_i and B.

Since we are in a regime where the motional Stark field can be large (due to high T_i and B), and since, with a B of several T, the magnetic perturbation of the field-free energy levels can approach the fine-structure separation, the motional Stark effect may in fact be more linear than quadratic in the magnetic field strength. As n increases, the Zeeman shift of a given m_j level

$$\Delta E_Z \approx m\mu_0 B \ , \tag{19}$$

becomes comparable to $\Delta E_{\rm FS}$ and the Paschen-Bach regime is attained. Thus states with $\Delta m = \pm 1$ can approach degeneracy with respect to the Stark perturbation. Ignoring the Zeeman splitting, the energy separation between previously degenerate levels with $j \simeq n/2$ due to an electric field F is given by[28]

$$\Delta E^L \approx 3\frac{\sqrt{3}}{4}\frac{n}{Z}\frac{4\pi\epsilon_0 a_0}{e^2}F\mathscr{R} \ . \tag{20}$$

Using the motional Stark field for F, and equating this shift to the minimal fine-structure separation gives

$$n_S^L \approx 1.91\left[\frac{Z^{11}}{T_i B^2}\right]^{1/12} \ , \tag{21}$$

as an estimate of the critical value of n at which l mixing due to the motional Stark field may become important. Again, a near linear dependence on Z and weak dependence on T_i and B are evident.

The critical n values for Stark mixing given by Eqs. (18) and (21) are plotted in Fig. 8, and the interpretation of the plots is similar to that for the collisional l-mixing

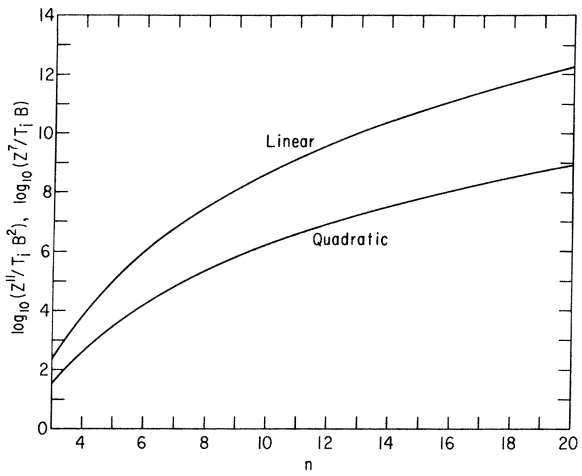

FIG. 8. Approximate n value for onset of l mixing due to motional Stark effect. Curves for both the linear and quadratic Stark effect estimates are shown. T_i is in keV and B in T.

case. For a given Z, T_i, and B, any n values to the right of the curve can be considered to have the l levels mixed while those to the left will be unmixed. Unlike the collisional case, the criteria for l mixing is not well defined. The two values of n_S in Fig. 8 are quite close to one another, and to evaluate the importance of Stark mixing compared to collisional l mixing, we take whichever is lower for given plasma conditions as our criteria for whether a given n state has significant Stark mixing. For T_i approximately a few keV, $B=2$ T, and $Z=2$–8, one readily concludes that collisional mixing is still the dominant process for causing a mixing of l-level populations at the lowest possible n values. However, it seems possible that Stark mixing may become important at conditions with high temperature, high field strength, and low density.

The consequences of severe l mixing on the rate coefficients for charge-exchange excitation are estimated by insisting that above some critical level n_c, given by Figs. 7 and 8, the l levels for a given n state are fully coupled [with relative populations $(2l+1)/n^2$] during the cascade process. For typical PDX parameters, we have $n_c \simeq 2$ for He^+, $n_c \simeq 5$ for C^{5+}, and $n_c \approx 6$ for O^{7+}, and the rate coefficients plotted in Figs. 2, 4, and 6 are recalculated and plotted in Figs. 9, 10, and 11 with statistical distributions imposed during the cascades for all $n \geq n_c$. For $n \geq n_c$ the preferred coupling of the low l levels to the lowest energy states and the strong coupling of all l levels to one another in the excited state causes a larger fraction of the electrons to drain through the $\Delta n > 1$ channels than would do so in the absence of l mixing. Likewise, a drop in excitation rates for $\Delta n = 1$ transitions out of the lower states occurs with l mixing at high n because the cascading electron distribution has shifted to lower l values and the $\Delta n > 1$ transitions are then energetically preferred. As can be seen by comparing Figs. 2–6 and 9–11, the overall effect of l mixing is to reduce the rate coefficients for most of the $\Delta n = 1$ transitions, especially for $n > n_c$.

The results presented here are necessarily qualitative due to the simple model used for l mixing, but they do illustrate the importance of more detailed studies of the influence of collisional mixing on CXRS. It is interesting to note that the $\Delta n > 1$ transitions can be most affected by l mixing. For example, at 25 keV/amu, the 7-3 transition in O^{7+} is 2.7 times more intense with l mixing than without while the 3-2 transition has a corresponding ratio of 0.65, resulting in an intensity ratio change of >4 above that expected without l mixing for $n \geq 6$.

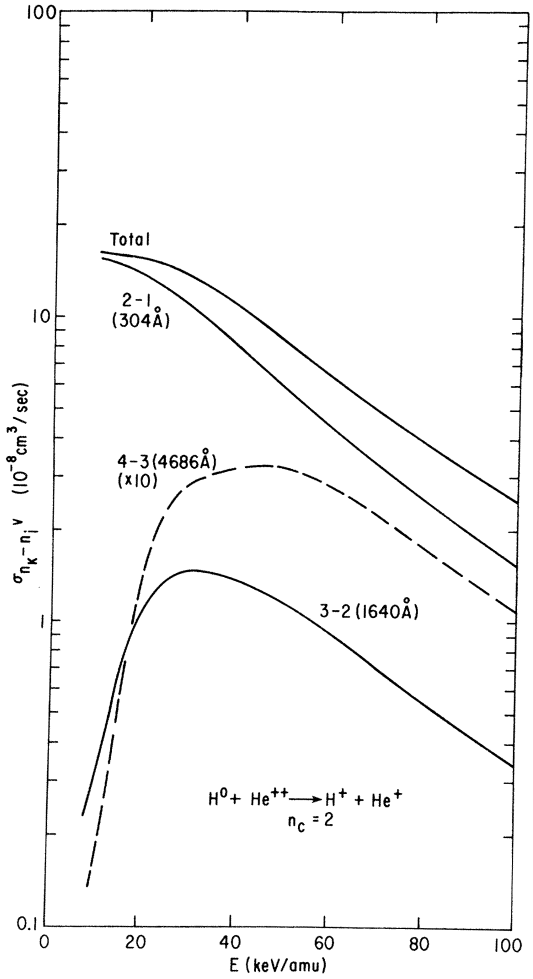

FIG 9. Excitation rate coefficients for $\Delta n = 1$ transitions in He^+ excited by charge exchange. The UDWA cross sections of Ref. 23 are used and full l mixing is assumed for $n \geq 2$.

A further consequence of the presence of l-mixing effects is the general principle that the lowest accessible $\Delta n = 1$ transitions are best suited for accurate fully stripped impurity density measurements using CXRS. This is so because the cascade process tends to wash out uncertainties in the (n,l) distributions at high n and hence the lower $\Delta n = 1$ transitions are least affected by a lack of precise knowledge of the direct (n,l) distributions and l-mixing effects at high n.

Finally, l-mixing processes can substantially alter the intensity of light emitted by the plasma due to electron excitation of the hydrogenic ions which will inevitably be present in the cooler plasma periphery. This radiation is at the same wavelength as that excited by prompt charge

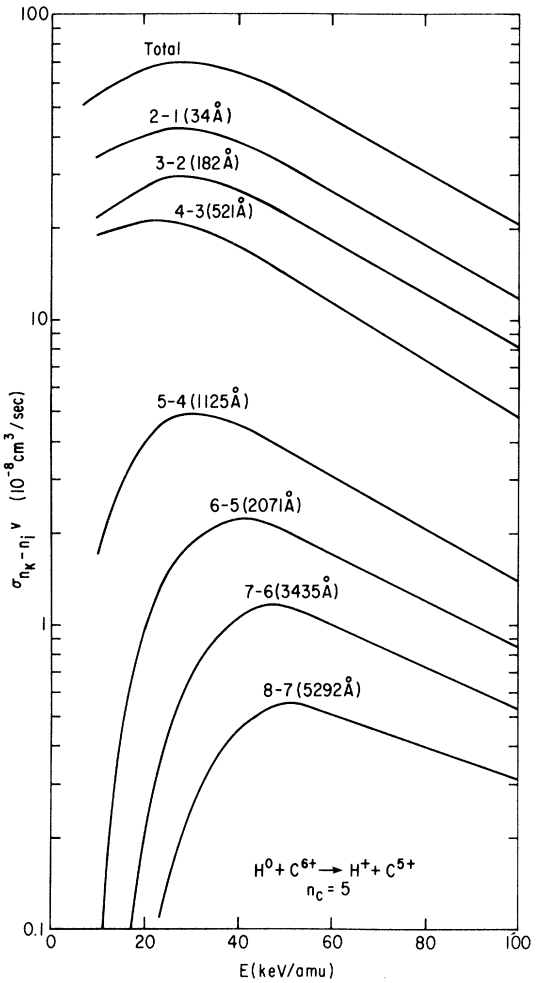

FIG. 10 Excitation rate coefficients for $\Delta n = 1$ transitions in C^{5+} with l mixing for $n \geq 5$. UDWA cross sections of Ref. 23 are used.

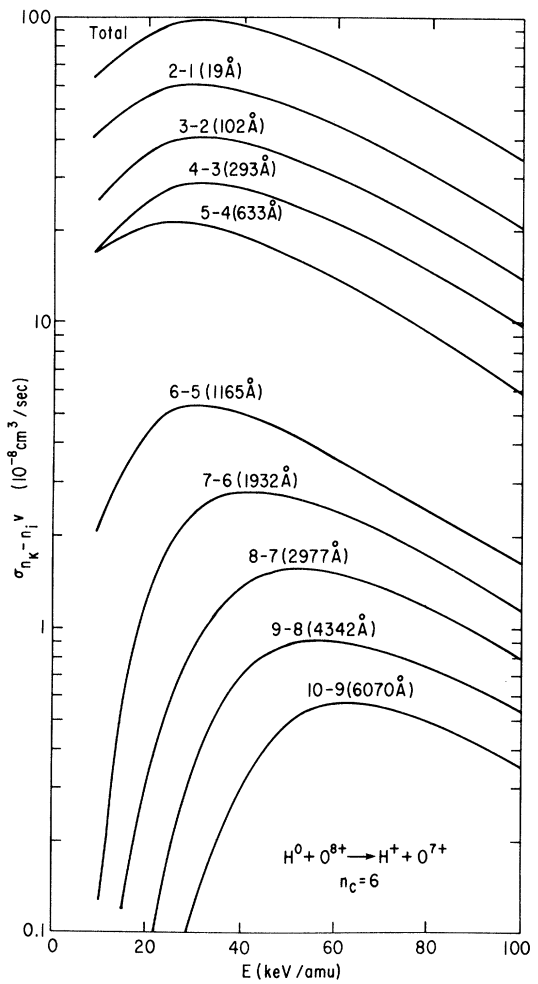

FIG. 11. Excitation rate coefficients for $\Delta n = 1$ transitions of O^{7+} with l mixing for $n \geq 6$. UDWA cross sections of Ref. 23 are used.

exchange, and it can be a source of considerable complication in interpreting signals from the spectrometer. Since electron excitation of high-n levels of C^{5+} and O^{7+} is weak (due to their high excitation energies from the ground state) whereas charge-exchange cross sections peak at large n, electron excitation of $\Delta n = 1$ lines in C^{5+} or O^{7+} is usually negligible with respect to prompt charge exchange at high-n values. Indeed, it is only with charge-exchange excitation that these transitions are observed easily in tokamak plasmas. However, for very-low-Z elements such as He or Li, the charge-exchange cross sections tend to peak at $n \approx 2$ and drop rapidly as n increases ($\sigma \sim 1/n^3$). The threshold energy for electron impact excitation of higher n levels is sufficiently small that electron excitation rates are comparable to charge-exchange rates, contrary to the case for higher Z. This is discussed in some detail later, but we note here that l mixing can significantly increase the electron impact excitation rate of $\Delta n = 1$ transitions by moving the excited electron from the $np\,^2P$ state (which will decay back to the ground state with high probability) to higher l levels which will then decay to intermediate levels. For example, the electron excitation of the He II 4-3 transition at 4686 Å via excitation of the $n = 4$ state from the ground state can be enhanced by about an order of magnitude if the $n = 4$ state is heavily mixed. This result has implications for the use of such transitions for ion temperature measurements and for the study of He^{2+} ash in tokamak devices, and will be referred to later. Of course, modulation of the neutral beam (as in Ref. 10) or spectral line profile discrimination (see Sec. V) can be used to distinguish between prompt charge-exchange radiation and background plasma light from the plasma edge, but the charge-exchange process itself creates ions which can be excited via electron impact and thus change the expected line intensity. Modulation of the beam will not help distinguish between the electron excitation component and the direct charge-exchange component.

III. FINE-STRUCTURE EFFECTS ON THE LINE PROFILE

The ability to determine the ion velocity distribution via CXRS depends on the line shape being determined

predominantly by Doppler effects. For an ion species with a Maxwellian distribution and temperature T_i in keV, the full width at half maximum (FWHM) of the Gaussian line shape is given by

$$\Delta\nu_D = \nu 1.73\times 10^{-3}(T_i/Z)^{1/2} \tag{22}$$

where ν is the wave number of the transition and the ion mass is taken to be $2Zm_p$. For $\Delta n = 1$ transitions in hydrogenic ions, the wave number of the emitted photons is given by Eq. (14) to be

$$\nu = \frac{2Z^2}{n^3}\mathscr{R} \tag{23}$$

for high-n values. Using Eqs. (19), (22), and (23) one can readily conclude that the unresolved Zeeman splitting is negligible compared to Doppler broadening for T_i approximately equal to a few keV and $B = 1$–5 T. Likewise, motional Stark broadening is almost always much less than the Doppler width. Although Zeeman and Stark broadening of a line are less than the total separation of fine-structure components for our range of n and Z, one has to evaluate whether the unresolved fine structure itself may give rise to incorrect temperature measurements. Any such effect will be most pronounced at low T_i where the Doppler broadening is small. Temperatures measured near the edge of the plasma will thus be most influenced by this effect. Even if the FWHM of a line profile gives a good measure of T_i, subtleties in the line wings can be mistakenly attributed to nonthermal ion velocities. To assess the magnitude of these effects, we calculate the total line profiles which arise from a superposition of Gaussian line shapes centered at the position of the fine-structure components. These profiles then allow us to calculate correction factors to be applied to T_i measurements when Eq. (22) is used to derive T_i from the FWHM. Since atomic fine structure is often the dominant broadening mechanism for the unresolved manifold of lines, we neglect Zeeman splitting and use the field-free energy levels.

The energy level of discrete (n,j) states of hydrogenic ions has been tabulated to high accuracy by Garcia and Mack[31] and we use these values to evaluate the wavelengths of all electric dipole transitions between states with $\Delta n = 1$. The relative intensities of given fine-structure transitions are obtained by using the cascade-corrected cross sections for excitation via charge exchange as given by Eq. (3) and including l mixing in higher n states where appropriate. The population of different j levels of the upper state is obtained from the cascade-corrected l distribution and the Burger-Dorgelo-Ornstein sum rule.[32] Samples of the resulting intensities and position of fine-structure components are shown in Fig. 12, along with the same transitions each having a Gaussian profile due to Doppler broadening. The sum of all the fine-structure components is the overall envelope and represents the actual measured profile. Using the FWHM of the composite line profile from such calculations, we define an apparent ion temperature given by Eq. (22) and this FWHM. The ratio of the real temperature to this apparent value gives the correction factor by which experimental values of T_i should be multiplied to arrive at the actual ion temperature. These ratios for all $\Delta n = 1$ transitions of interest of He^+, C^{5+}, and O^{7+} are shown in Figs. 13–15 for beam energies of 25 keV/amu, and using the

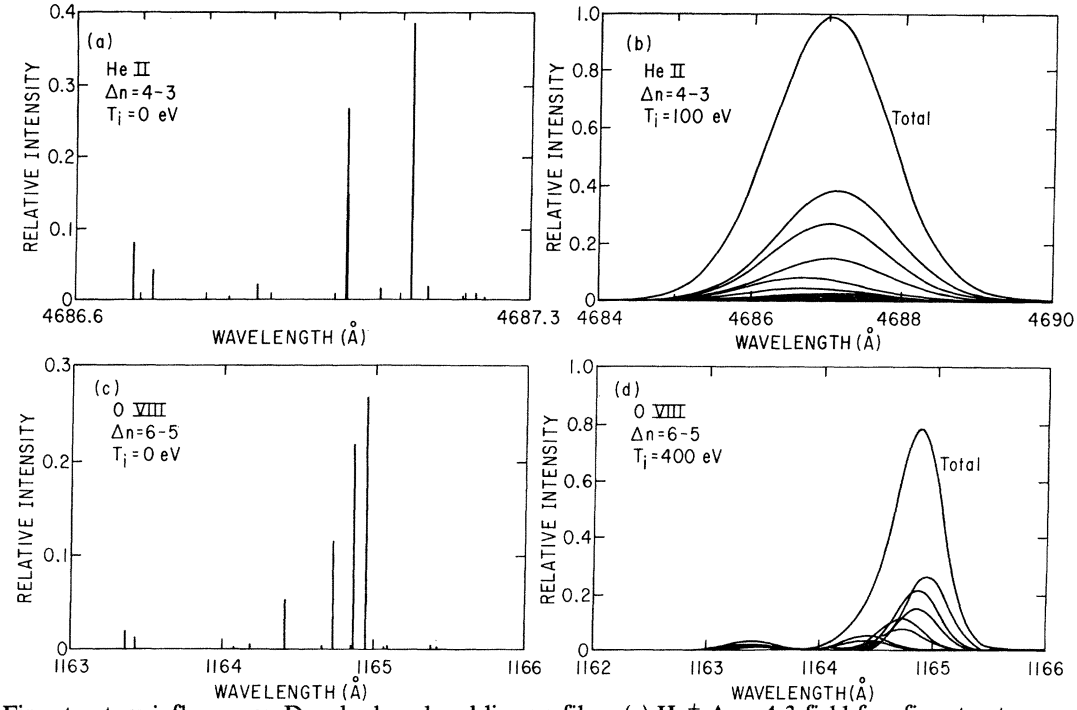

FIG. 12. Fine-structure influence on Doppler broadened line profiles. (a) He^+ $\Delta n = 4$-3 field-free fine-structure components; (b) same as (a) with Doppler broadened profiles at $T_i = 100$ eV; (c) O^{7+} $\Delta n = 6$-5 field-free fine structure; (d) same as (c) with $T_i = 400$ eV.

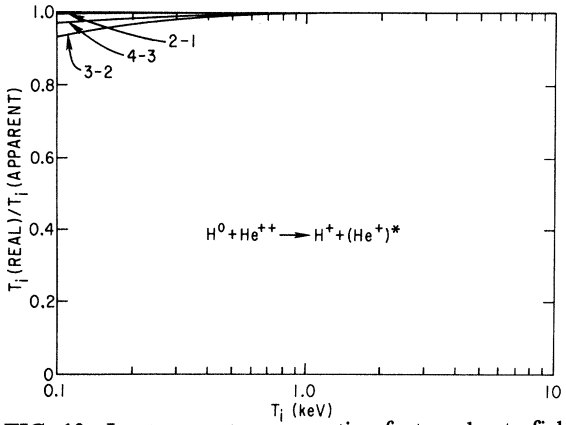

FIG. 13. Ion temperature correction factors due to field-free fine structure for He^+ with excitation by neutral hydrogen. Complete l mixing is assumed for $n \geq 2$. The abscissa is the value of the real ion temperature, not the apparent value.

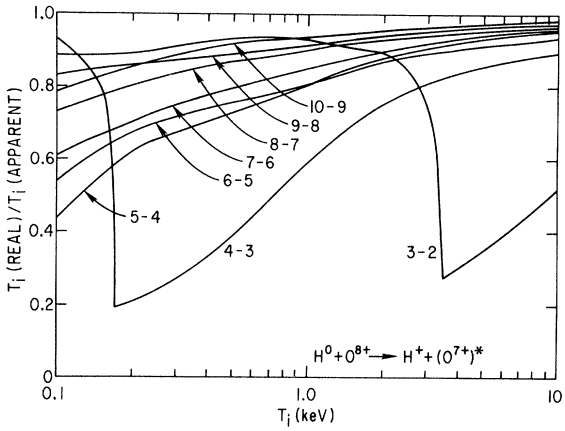

FIG. 15. Ion temperature correction factors due to fine structure for O^{7+} with excitation by 25-keV/amu neutral hydrogen. Complete l mixing is assumed for $n \geq 6$.

$\sigma_d(n,l)$ values of Ryufuku.[23] Full l mixing was assumed for $n \geq n_c$, where $n_c = 2$, 5, and 6 for He^+, C^{5+}, and O^{7+}, respectively. The large discontinuities in the curves for some transitions (e.g., 3-2 of C^{5+}) are due to the merging of the profiles of discrete fine-structure transitions as T_i increases and the Doppler width becomes larger than the transition separation. The closer the correction factor is to 1.0, the more symmetric and Gaussian-like the sum profile is. In general, the higher wavelength transitions are least susceptible to distortion by fine structure at high T_i and thus most suited for determining T_i. These results can change by up to $\sim 10\%$ depending on whether l mixing is included in the upper levels or not. The l mixing tends to broaden the line structure by increasing the intensity of widely separated fine-structure components originating from moderate to low l levels. However, since the high-n transitions which are preferred for T_i measurements are also those which originate from transitions out of l-mixed states, these curves provide a reasonable correction factor for T_i measurements which can be applied over a very wide parameter range.

A few obvious conclusions can be drawn from these results. The low-lying transitions are not well suited for ion temperature measurements unless the fine-structure components themselves are resolved. Transitions between high n states are much better but, as noted earlier, the charge-exchange cross sections drop rapidly as n increases. Helium is almost ideal due to its low mass and relatively bright visible line, but this 4-3 transition is best excited by neutral beams with a high primary beam energy ($\gtrsim 60$ keV/amu) so that all three beam energy components contribute to the CXRS signal. On the other hand, measurements using helium are most prone to errors arising from recombined ions drifting into the spectrometer line of sight (see the next section). The visible lines of C^5 and O^{7+} are also attractive candidates except that, again, higher beam energies are desirable for reasonable intensities. Also, overlap with visible lines of H I and other impurity ions tends to make several of these lines questionable for reliable ion temperature measurements in the visible range unless the beam is modulated. The (60—90)-keV/amu beam energies planned for large tokamaks such as TFTR may make these lines quite attractive for simple fiber optically coupled spectrometer systems. For smaller tokamaks with (20—50)-keV/amu neutral beams, the near-uv lines of C^{5+} and O^{7+} are most attractive for ion temperature measurements when He^{2+} is not present in the plasma.

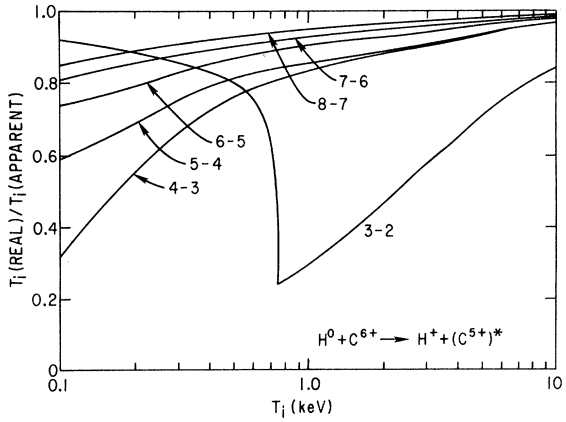

FIG. 14. Ion temperature correction factors due to fine structure for C^{5+} with excitation by 25-keV/amu neutral hydrogen. Complete l mixing is assumed for $n \geq 5$.

IV. RADIATION FROM PRODUCT IONS

Finally, we consider the effects of hydrogenic ions which are produced by the neutral beam out of the spectrometer line of sight and subsequently drift into the sightline as they follow the magnetic field lines. Consider a typical experimental situation as depicted in Fig. 16, wherein a neutral beam is injected in the toroidal plasma midplane with a tangency radius of R_{BT}. A spectrometer sightline, also in the plasma midplane, with tangency radius R_{ST} intersects the beam at a major radius of R_I. Since hydrogenic ions are produced via reaction equation (1) along the entire beam line, there is a source of hydrogenic ions at all R that may be able to drift around the

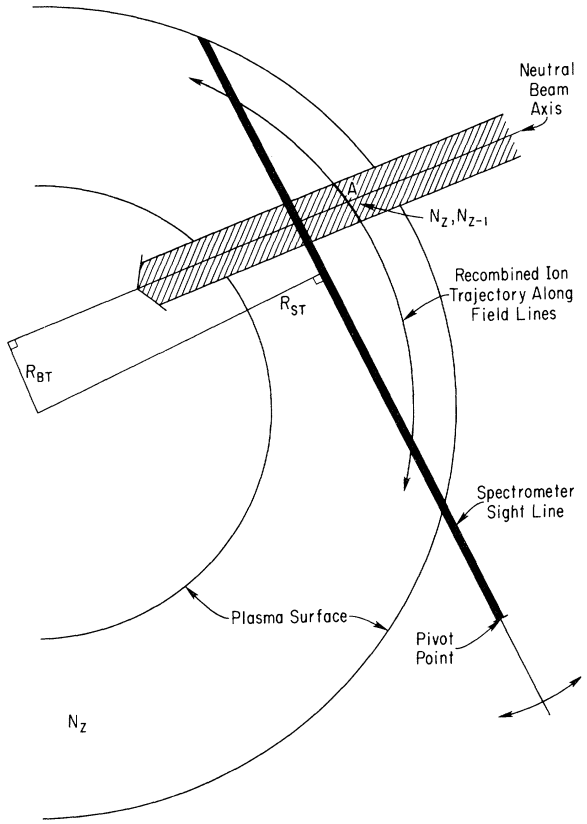

FIG. 16. Typical experimental geometry for CXRS measurements on the PDX tokamak. Both the neutral beam and the spectrometer line of sight are in the plasma horizontal midplane.

torus into the view of the spectrometer. For example, ions with charge $Z-1$ created in the beam volume near point A in Fig. 16 can follow the indicated trajectory to cross the spectrometer sightline before being ionized back to charge state Z. If the emission due to electron collisional excitation of these drifting ions, integrated along the spectrometer sightline, is comparable to the localized prompt charge-exchange emission at $R=R_I$, an erroneous ion velocity distribution (and/or fully stripped impurity density) will be derived since one is sampling ions created over a large range of R. This problem is most severe for lower-Z elements since the excitation energies of the charge-exchange-induced transitions are very low. It is especially relevant for measuring thermal He ash densities or for CXRS temperatures based on He^{2+}. Unlike interfering radiation from the cool plasma periphery, this electron excited component from radii different from R_I cannot be discriminated against by modulating the beam since it will be in phase with the beam just as the prompt charge-exchange signal will be.

An estimate of the magnitude and radial extent of the electron excited signal is given by a relatively simple model. The intensity of light at wavelength λ due to electron excitation out of the ground state is given by

$$B_\lambda^{e^-}=\frac{1}{4\pi}\int_L N_e(R)N_{Z-1}^{cx}(R)Q_{1s\text{-}np}^{Z-1}(R)b_\lambda dl\ , \qquad (24)$$

where $Q_{1s\text{-}np}$ is the electron excitation rate for the $1s$-np transition, b_λ is the branching ratio for the transition of interest, and N_{Z-1}^{cx} is the density of ions produced by charge exchange between the beam neutrals and ions with charge Z at a radius R. The integral in Eq. (24) is along the entire path that the spectrometer line of sight takes through the plasma. (For ease of calculation, we treat all plasma parameters as a function of major radius R.) We express N_{Z-1}^{cx} as a function of the value it attains in ionization charge-exchange equilibrium in the beam volume:

$$N_{Z-1}^{cx}=\xi(R)\frac{N_Z(R)}{N_e(R)I_{Z-1}(T_e)}\sum_{j=1}^{3}N_j\langle\sigma v\rangle_j^T\ , \qquad (25)$$

where N_Z is the density of ions with charge state Z at a major radius of R, N_e is the electron density, $I_{Z-1}(T_e)$ is the ionization rate coefficient for the $Z-1$ ion species, N_j is the density of beam neutrals with energy $E_0/\sqrt{j}$, and $\langle\sigma v\rangle_j^T$ is the total recombination rate coefficient of the Z ion species due to charge exchange. The proportionality factor $\xi(R)$ depends on the parallel transport of the recombined ions along the field lines and the particular beam-spectrometer geometry being used, and is discussed in more detail below. Since we are usually interested in fully stripped low-Z impurities in hot plasmas, it is reasonable to assume that N_Z is roughly proportional to the electron density, $N_Z(R)=N_e(R)\times\text{const}$.

Assuming a relatively narrow neutral beam so that the integral in Eq. (2) can be replaced by average values, the ratio of the radiation due to the ions drifting into the spectrometer sightline (which we henceforth refer to as the ion "plume" intensity) to the prompt charge-exchange signal at the same wavelength is given by

$$\frac{B_\lambda^{e^-}}{B_\lambda^{cx}}=\frac{1}{N_e(R_I)\sum_{j=1}^{3}[(Nl(R_I))_j\langle\sigma v\rangle_j^\lambda]}\times\int_L N_e(R)\xi(R)\frac{Q_{1s\text{-}np}^{Z-1}(R)b_\lambda}{I_{Z-1}(T_e)}\times\left[\sum_{j=1}^{3}N_j\langle\sigma v\rangle_j^T\right]dl\ . \qquad (26)$$

Note that this ratio is independent of the beam power since N_j is in both the numerator and denominator. Hence this plume emission can be significant even if the power itself is not sufficient to change the overall ionization balance of the impurities. That this ratio can easily be significant may be seen by noting that, at least for 2-1 transitions, the electron excitation rate roughly equals the ionization rate while the total charge-exchange rate is always greater than or equal to the rate for exciting a given transition. The plume-to-prompt ratio then reduces approximately to the ratio of N_e, weighted by ξ and integrated along the entire spectrometer line of sight, to the value of N_e at the intersection point times the beam width.

The plume attenuation factor $\xi(R)$ is estimated by con-

sidering the transport of ions along the magnetic field lines. This problem has been addressed by Clark *et al.* for the DITE tokamak[33] for the general case where parallel diffusion is sufficiently slow that toroidal asymmetries in the impurity ion distribution can be sustained. We follow their treatment of the problem but restrict our discussion to plasmas where $T_e \gtrsim 1$ keV and $Z_{\text{eff}} \lesssim 2$ so that over most of the plasma, the impurity ions are relatively collisionless. That is, the collisional mean free path is $\gtrsim 2\pi R_{Pl} q$ where R_{Pl} is the plasma major radius and q is the safety factor due to the rotational transform of the magnetic field. This assumption is usually valid for neutral beam heated plasmas, and it allows us to obtain a simple expression for $\xi(R)$.

Ignoring the rotational transform of the field for the moment, we consider a one-dimensional model for the ion motion along the field line. Referring to Fig. 17, we let S denote the displacement along a field line and, for $-d < S < d$, a neutral density from a neutral beam induces charge-exchange reactions between the beam neutrals and impurity ions with density N_Z to produce particles with density N_{Z-1}. The length of the field line around the torus is taken to be $2L$. Taking ionization and charge-exchange recombination to be the dominant atomic processes (which is easily the case for He, and less valid for O), the continuity equations for particles moving in the $+S$ direction are

$$v\frac{\partial N_{Z-1}}{\partial S} = \frac{N_Z}{\tau_{\text{cx}}} - \frac{N_{Z-1}}{\tau_i} , \quad -d \le S \le d \tag{27a}$$

$$v\frac{\partial N_{Z-1}}{\partial S} = -\frac{N_{Z-1}}{\tau_i} , \quad L \ge |S| \ge d , \tag{27b}$$

where $\tau_i = N_e I_{Z-1}$ is the electron impact ionization time and $\tau_{\text{cx}}^{-1} = \sum n_j \langle \sigma v \rangle_j^T$. For simplicity, we also assume that the ionization distribution is not drastically changed so that we may take the density of fully stripped ions, N_Z, to be constant. Expressing the density as a fraction of the value obtained in equilibrium in the beam region

$$\xi \equiv \frac{N_{Z-1}}{N_Z}\frac{\tau_{\text{cx}}}{\tau_i} , \tag{28}$$

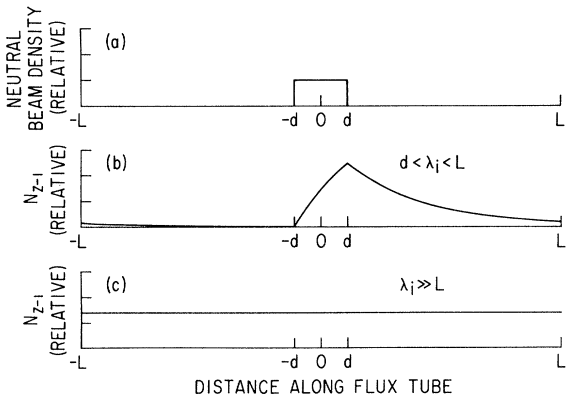

FIG. 17. One-dimensional geometry for drifting ion plume calculations. (a) Neutral beam density as a function of distance along the field line; (b) relative density of recombined ions moving in the + direction for $L = 3\lambda_i = 9d$; (c) relative density of recombined ions for $\lambda_i \gg L$.

we use continuity at $|S| = d$ and $|S| = L$ to solve for ξ, which is just the plume attenuation factor of interest. The general solutions are

$$\xi_+(S) = 1 - \frac{\sinh[(L-d)/\lambda_i]}{\sinh(L/\lambda_i)} e^{-S/\lambda_i} \tag{29a}$$

for $d > S > -d$, and

$$\xi_+(S) = \frac{2\sinh(d/\lambda_i)}{1-e^{-2L/\lambda_i}} e^{-S/\lambda_i} \tag{29b}$$

for $L \le S \le d$, and

$$\xi_+(S) = \frac{2\sinh(d/\lambda_i)}{1-e^{-2L/\lambda_i}} e^{-(2L+S)/\lambda_i} \tag{29c}$$

for $-d \le S \le -L$. Here $\lambda_i = v\tau_i$ is the ionization mean free path for particles with velocity v. We have taken $v = (2kT/\pi m)^{1/2}$, but in the very collisionless case, the ξ_+ could equally well be integrated over a Maxwellian distribution. This only changes the final result by about a factor of 1.5 or so at most. The + subscript on ξ indicates that we have considered only particles going in the $+S$ direction, and there is an identical population going in the $-S$ direction that must also be included. Putting these results in the context of our experimental situation, we have $L \simeq \pi R q$, while S represents the arc length around the torus between the neutral beam center and the spectrometer sightline at a given R, and $2d$ is the intersection length of a magnetic flux tube through the neutral beam at R.

We consider two limiting cases of practical interest. For very low Z, such as He^+, it is usually true that $2d \ll \lambda_i \ll L$. That is, the hydrogenic ions are reionized to the fully stripped state before going once around the torus (hence the term ion plume). Here the negative-going ions never reach the spectrometer line of sight and the plume attenuation factor becomes

$$\xi(S) \approx \frac{d}{\lambda_i} e^{-S/\lambda_i} \quad (S > d) . \tag{30}$$

Then for $S \ll \lambda_i$ (i.e., for points on the spectrometer sightline near the beam), the plume attenuation factor is just one-half the beam width along the flux tube divided by the ionization mean free path. For higher Z such as oxygen, the limit $2d \ll L \ll \lambda_i$ is more applicable and we have

$$\xi(S) \approx \frac{d}{L} \tag{31}$$

which is just a simplified case of the ions being in ionization-charge-exchange equilibrium around the torus but with the neutral beam density being the volume averaged neutral density instead of the local beam density. This is just the expected limit for $\lambda_i \gg L$.

It is the short λ_i limit that gives the greatest ion plume intensity contribution, and hence the problem in general will be more severe for He than C or O. We note, however, that since $\lambda_i < \pi R$, the hydrogenic ions do not circle the torus before ionizing and the spectrometer line of sight through the ion plume can be minimized by viewing

vertically instead of in the horizontal midplane or, conversely, the beam could inject vertically.

We have calculated the ion plume to prompt charge-exchange intensity ratio given by Eq. (26) for cases of interest on the PDX and TFTR tokamaks to illustrate typical results. A computer code calculates the expression in Eq. (26) using Eqs. (29) as appropriate to account for all intersections of the neutral beam and spectrometer sightline with a given flux surface of major radius R. Before discussing the results, we note two subtleties of the calculations. The first is that presence of l mixing in excited states can increase the branching ratio drastically above that with no l mixing, resulting in a greatly enhanced plume intensity. For example, the He II 4686-Å (4-3) line is increased by a factor of 7 by the presence of l mixing when excited from the ground state by electron impact, as previously mentioned in Sec. II. The second point is that the field lines in a tokamak do in fact have a nonzero rotational transform and, depending on the beam height, spectrometer viewing geometry, and the separation along a flux tube between the beam and spectrometer sightline, the ion plume can rotate around the center of the plasma and not cross the spectrometer sightline at all. This of course assumes that cross field transport within the flux surface is negligible. We account for this in our calculations by assuming $B_p/B_T \approx a/q(a)R$ for all r down to some r near the plasma center, where $r = R - R_{pl}$ is the minor radius of a given flux surface, B_p is the poloidal field strength and B_T is the toroidal field strength. Given this tilt of the magnetic field lines, the contribution to the integral in Eq. (26) at a given R is set to zero if the vertical separation between the beam center and the spectrometer sightline is greater than one-half of the nominal beam height. The assumption of a constant B_p/B_T down to some cutoff r is roughly consistent with the rotational transform as a function of r calculated for several PDX cases using measured N_e and T_e profiles as a function of time and solving the magnetic diffusion equation to derive $B_p(r,t)$. Although relatively crude, these assumptions allow us to get first-order estimates of the plume intensity and spatial distribution. The calculations are most uncertain for the cold plasma edge where the assumption of collisionless parallel transport is no longer valid.

For the sample cases for TFTR and PDX, we set the position of the neutral beam and vary the tangency radius of the spectrometer sightline to scan the intersection region in R. Parabolic density profiles with the temperature profiles proportional to the square of the density profile are assumed for both cases. $R_{pl}=145$ cm, $a=40$ cm, $N_e(0)=4\times10^{13}$ cm^{-3}, and $T_e(0)=1.5$ keV are used for the PDX example while the TFTR case has $R_{pl}=250$ cm, $a=80$ cm, $N_e(0)=5\times10^{13}$ cm^{-3}, and $T_e(0)=1.5$ keV. The safety factor $q(a)$ at the plasma edge is taken to be 3 for both cases and a full beam height of 16 cm is assumed for PDX and 40 cm for TFTR. The distinguishing feature between the two cases is that the beam injection angle in PDX is near perpendicular with a 35-cm tangency radius while in TFTR the injection is nearly tangential with a tangency radius of 230 cm. The toroidal separation in the plasma midplane between the spectrometer pivot point and the location of the beam source is taken to be 56° in the PDX cases and 78° in TFTR, both values chosen to reflect actual experimental setups. A horizontal beam width of 16 cm is assumed for PDX and 20 cm for TFTR, while a primary beam energy of 22 or 44 keV/amu (44 kV D^0 or H^0) is used for PDX and 90 keV/amu (H^0) is assumed for TFTR. For comparison, the 90-keV/amu case is calculated for PDX also. The beam species ratio is assumed to be 2:1:1 for both cases. Charge-exchange rates from Figs. 9—11 are used along with electron impact excitation rates obtained by Mewe[34] and electron ionization rate coefficients from Bell *et al.*[35] Both the neutral beam and spectrometer are assumed to be in the plasma midplane.

The plume-to-prompt intensity ratio is plotted as a function of the neutral beam-spectrometer sightline intersection radius for these two cases in Figs. 18 and 19 for a few transitions of interest. These results show a few general features that merit mentioning. The drop with beam energy reflects the increase in the charge-exchange excitation rate of these Rydberg transitions as the beam energy increases. In fact, the 90-keV/amu energy assumed for the TFTR case accounts for most of the reduced ratio for

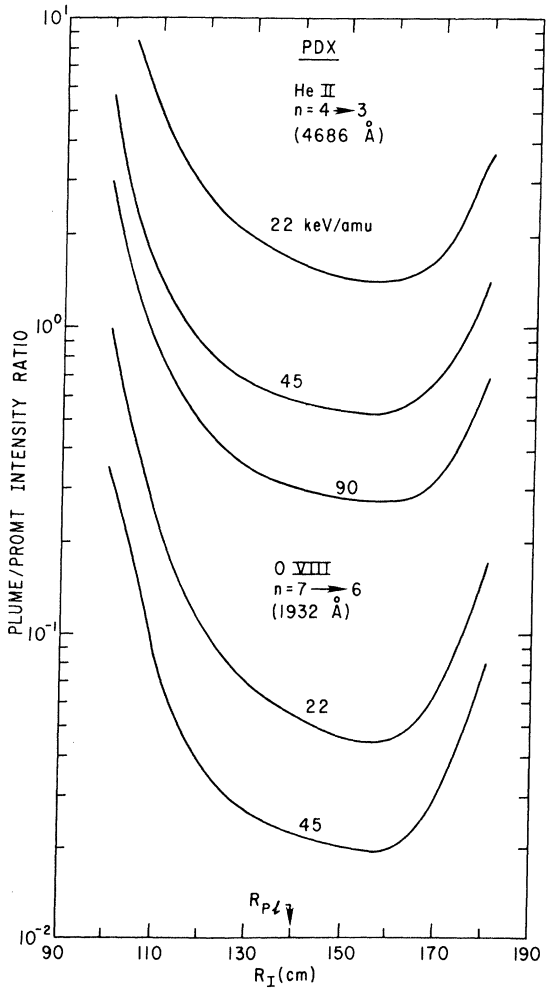

FIG. 18. Plume-to-prompt intensity ratios for the PDX geometry with near perpendicular beam injection ($R_{BT}=35$ cm, $R_{pl}=140$ cm, $a=40$ cm).

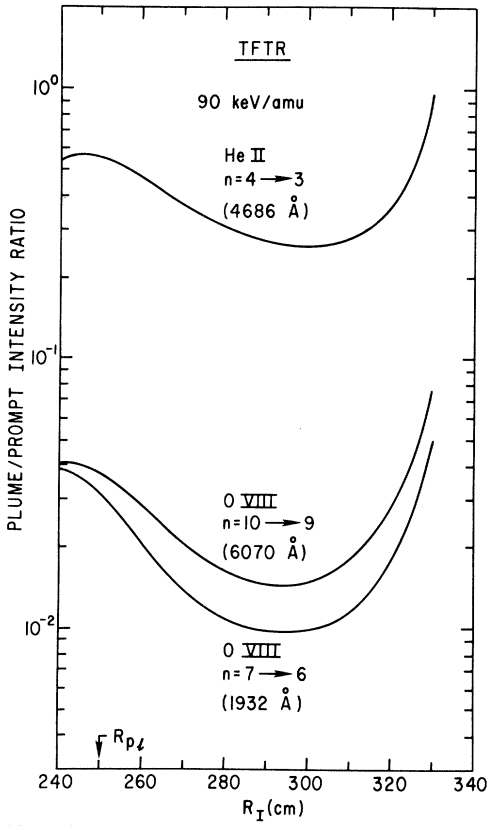

FIG. 19. Plume-to-prompt intensity ratios for the TFTR geometry with tangential injection ($R_{BT}=230$ cm, $R_{Pl}=250$ cm, $a=80$ cm).

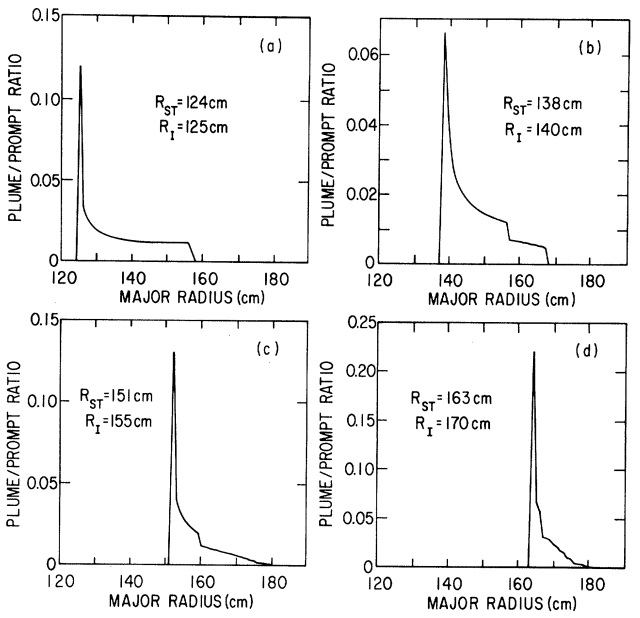

FIG. 20. Plume-to-prompt intensity ratio distribution as a function of major radius for the PDX case with 45-keV/amu hydrogen excitation of He^+ 4686 Å ($\Delta n=4$-3). R_{ST} is the tangency radius of the spectrometer sightline while R_I is the beamline-spectrometer sightline intersection radius. $R_{Pl}=140$ cm and $a=40$ cm.

He^+ seen in Fig. 19 compared to the He^+ cases in Fig. 18. This is evident from a comparison of the 90-keV/amu case to the lower energy cases in Fig. 18. Also, the similarity in the ratio for the $\Delta n=10$-9 O VIII transition and the 7-6 O VIII transition is due to the rapid drop ($\sim 1/n^3$) in both the charge-exchange and electron impact rates as n increases.

As expected, the plume-to-prompt ratio is largest for the He^+ cases, and often is negligible for the O^{7+} transition. When the beam energy is low, only the C^{5+} and O^{7+} Rydberg transitions will be relatively unpolluted by plume intensity and hence are preferred for ion temperature measurements even though they are in the uv instead of visible spectral regions (the visible Rydberg transitions are often not sufficiently excited at low energies). As mentioned earlier, the He^+ case can be improved upon by viewing vertically with the spectrometer or neutral beam so that the path length through the drifting ion population is minimized.

When the drifting ion plume intensity is comparable to the prompt charge-exchange signal, it affects the ion velocity distribution measurements only insofar as the plume has nonzero intensity at radii different from the intersection radius so that the source is no longer localized. Examples of the radial distribution of the He^+ plume intensity ratio are shown in Fig. 20 for the 45-keV/amu case of Fig. 18. In general, the maximum contribution comes from the tangency radius of the spectrometer sightline where the path length through a flux tube is maximized. Depending on the particular experimental setup, this can be quite different from R_I, the intersection radius. For $R_I < R_{Pl}$ the spatial extent of the plume intensity is quite large and hence more reliable T_i values can be expected for $R_I > R_{Pl}$. Even then, one should correct the value of R to which a measured T_i is assigned by estimating a value weighted by the prompt and plume intensities. It should be noted that the sharp discontinuities in the plume profiles at large R in Fig. 19 are artifacts in the calculation due to the assumption of a rectangular profile of the beam intensity in the vertical direction. The reduction in intensity as the magnetic field lines rotate the plume out of the spectrometer sightline thus shows as an abrupt drop instead of a more realistic gradual decrease.

In general, the plume intensity should be checked for each case and geometry of interest, since beam properties, plasma parameters, and experimental conditions all influence the plume-to-prompt ratio. It is most important for lowest-Z elements, such as He and Li, and for the resonant 2-1 transitions for all elements since the electron excitation rate for these transitions is a maximum for a given element. Thus it will be of considerable importance in CXRS measurements of thermalized He ash and in low-Z impurity transport experiments which employ the 2-1 transitions in order to exploit their high intensities under charge-exchange excitation.

V. EXPERIMENTAL RESULTS

Observations have been made on the PDX tokamak to illustrate ion velocity distribution measurements using

CXRS. A schematic of one of the experimental setups used is shown in Fig. 21. Here, one of the main heating beams is used as the fast neutral source. Each beamline (out of a total of four on PDX) injects near perpendicularly into the torus with a primary beam energy of 40—46 keV and total power of 1.0—1.5 MW. For these experiments, the neutral beam viewed by the spectrometer (designated by its geographical location on the torus) was not modulated, but since the beams do not overlap, spatially localized measurements are still possible. The beamline has a FWHM of 16—20 cm in the plasma center, and a spatial resolution of $\lesssim 10$ cm centered on the intersection volume is available when the spectrometer field of view and beam width are taken into account. Both the beamline and spectrometer sightline lie in the plasma midplane.

Light collected by the collimating lens is transmitted by a quartz fiber optic bundle to the remote spectrometer. Only the small collimating telescope with an associated scanner drive is physically near the tokamak. The major radius of the intersection region of the beam and spectrometer sightline was varied on a shot-to-shot basis by rotating the collimating telescope at the window port.

As shown in Fig. 21, a 0.5-m focal length spectrometer with a rapid scanning mirror on the exit slit assembly is used to obtain a short-range spectral scan across the line profile every 50 ms. While this system is extremely simple, it has the disadvantage of relatively low efficiency, and an optical multichannel analyzer is preferred for high time resolution with reasonable signal-to-noise ratios.

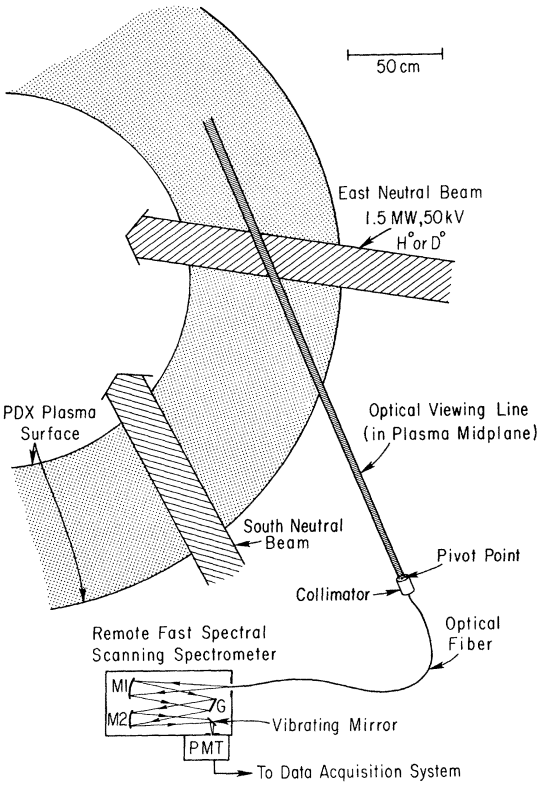

FIG. 21. Schematic of experimental setup on PDX for CXRS measurements.

The measurements reported here were made during a series of runs studying the high confinement regime (H mode)[36] in a single null divertor configuration.[37] Typical plasma parameters were $T_e(0)=1.5$—2.0 keV, $\bar{N}_e=1$—4×10^{13} cm^{-3}, $I_p=400$ kA, $R_{Pl}=140$ cm, and $a=40$ cm. The neutral beams were either H^0 or D^0, and the plasma working gas was D^+ except during a short run with a He^{2+} plasma. Typical total beam power injected was 2—3 MW, which required two D^0 or three H^0 beams. Plasma discharge lengths were 900 ms with beam injection for 300 ms.

Spectral profiles of the He II 4686-Å line with and without the neutral beams are shown in Fig. 22 for the $H^0\rightarrow D^+$ case. A broad component is evident when the east beamline is on, and this feature is caused predominantly by charge-exchange excitation of the He^+ in the beam-spectrometer intersection region. The narrow component is due to electron impact excitation of He^+ at the cool plasma periphery and is present even when the neutral beam is off [cf. Fig. 22(a)]. The increased noise level during neutral beam heating is due to instabilities in the plasma edge in H-mode discharges and neutron-induced noise in the photomultiplier.

The He II 4686-Å ($\Delta n=4-3$) line was used for these measurements because the beam energy was usually too low to sufficiently excite the high Rydberg transitions of

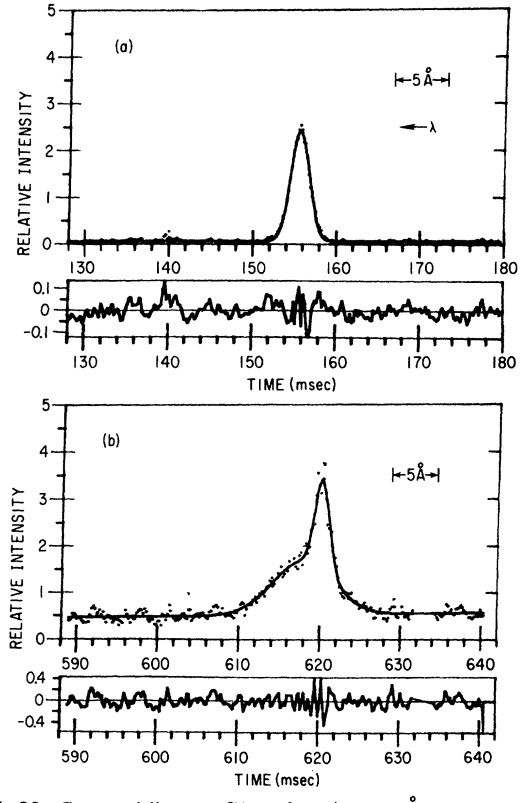

FIG. 22. Spectral line profiles of He^+ 4686-Å line from PDX ($H^0\rightarrow D^+$). (a) Neutral beam off with data fitted to a single Gaussian profile (solid line) with a linear background; (b) neutral beam on with data fitted to a sum of two Gaussians (solid line) and a linear background. The residual differences between the data and the fitted functions are shown below each data sample. A change in time is equivalent to a linear change in wavelength.

O^{7+} and C^{5+}. With a 45-keV/amu H^0 beam, the $\Delta n = 10-9$ O VIII transition at 6070 Å was observed during beam injection but with intensities too low for reliable line profile measurements. Some of the low intensity was due to poor sensitivity of the grating above 5500 Å. Helium was present in the plasma in concentrations of a few percent of the electron density, the source being both leakage of He into the discharge from several neutral particle energy analyzers and a small addition of He to the prefill gas.

For the experimental arrangement shown in Fig. 21, only H^0 beams provide useful T_i measurements because the charge-exchange excitation of He II 4686 Å is quite weak with 22-keV/amu D^0 beams and a large amount of He^{2+} is required for good signal strength. In addition, the central plume-to-prompt ratio is estimated to be > 1.2 for the D^0 beam with typical plasma parameters. This ratio is reduced to 0.3—0.4 for the H^0 beam, and about half of this plume intensity originates at radii within ± 5 cm of the intersection radius.

The ion temperature and toroidal rotation velocity are determined from the measured line profiles by using a nonlinear least-squares-fitting procedure to fit a double Gaussian function to the measured profile. A polynomial is included in the fitting function to account for a time varying background intensity. The resulting fits for the data in Fig. 22 are shown by the solid lines. The residual difference between the fitted function and data is shown for each case. The instrumental profile of the spectrometer is roughly Gaussian with a FWHM of ~ 1 Å. The width of the broad component gives the ion temperature in the intersection volume while the separation between the centers of the narrow and broad components gives the toroidal rotation speed with respect to the plasma edge. Uncertainties in the derived values of v_ϕ and T_i due to both statistical uncertainties in the fits and shot-to-shot variations are included in the final uncertainty estimates. Shot-to-shot variations were dominant for these runs. The transition to the *H*-mode regime, characterized by a spontaneous and rapid rise in the plasma density, occurred at times in the discharges that varied over a 50-ms range (from 510—560 ms), which further increased the shot-to-shot variations. An estimate of the temperature near the plasma edge at $R = 180$ cm is derived from the width of the narrow spectral component.

The resulting ion temperature and rotation velocity profiles for these discharges are shown in Figs. 23 and 24 for three times in the discharge. The error bars shown indicate estimates derived from combining the uncertainties in the fit parameters with uncertainties from shot-to-shot variations obtained from repeated shots with $R_I = 145$ cm. Central values of T_i determined by passive charge-exchange measurements of the neutral particle energy spectrum[38] are also indicated. The CXRS and passive charge-exchange values agree within their estimated error bars.

The values of T_i and v_ϕ rise rapidly during the early phase of neutral injection ($t \approx 400-450$ ms), and small variations in the neutral injector timing and the spectrometer scanner phase can give rise to larger uncertainties in $T_i(r)$ and $v_\phi(r)$ at early times. The T_i and v_ϕ profiles broaden substantially after the transition to the *H*-mode phase of the discharge, and they indicate sharper gradients near the plasma edge (cf. $t = 660$ ms in Fig. 23). This qualitative behavior is characteristic of other plasma properties [e.g., $N_e(r)$, $T_e(r)$] in *H*-mode discharges. A residual plume intensity may cause a slight decrease in the measured T_i near the plasma center, especially during the low-$\bar{N}_e$ *L*-mode phase of the discharge (i.e., $t = 510$ ms), but should be less important at later times as N_e and T_e rise and hence shorten the He^+ ionization path length. The radial resolution in this initial data set is just marginally acceptable and may contribute to the high-

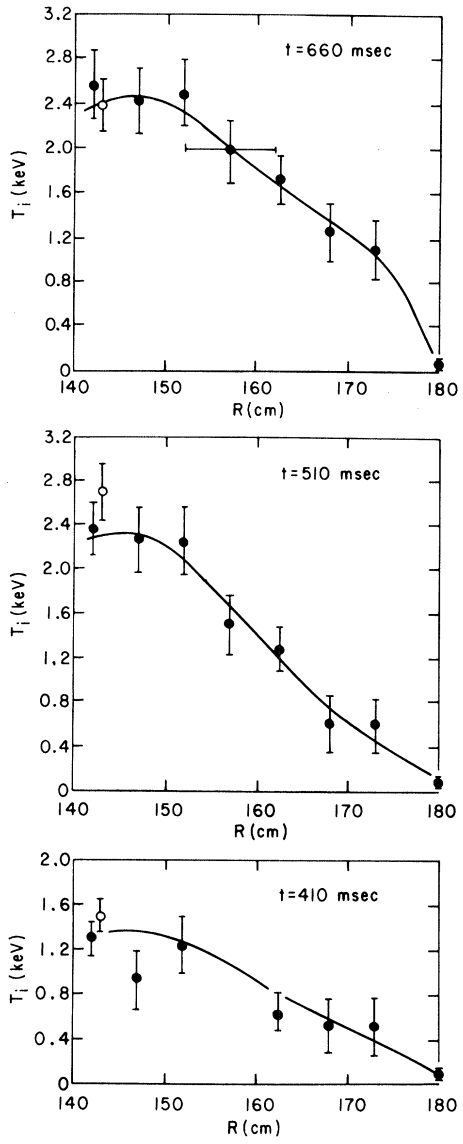

FIG. 23. Radial profiles of ion temperature for $H^0 \rightarrow D^+$ PDX plasma at three times during the discharge. Closed circles, CXRS measurements; open circles, passive charge-exchange results. Beam injection from $t = 400-700$ ms with $P_{\text{absorbed}} = 1.5-2.0$ MW. Transition to the *H* mode occurred between 520 and 550 ms for all shots. The plasma edge is at $R = 180$ cm while the plasma magnetic axis is at $R = 146$ cm.

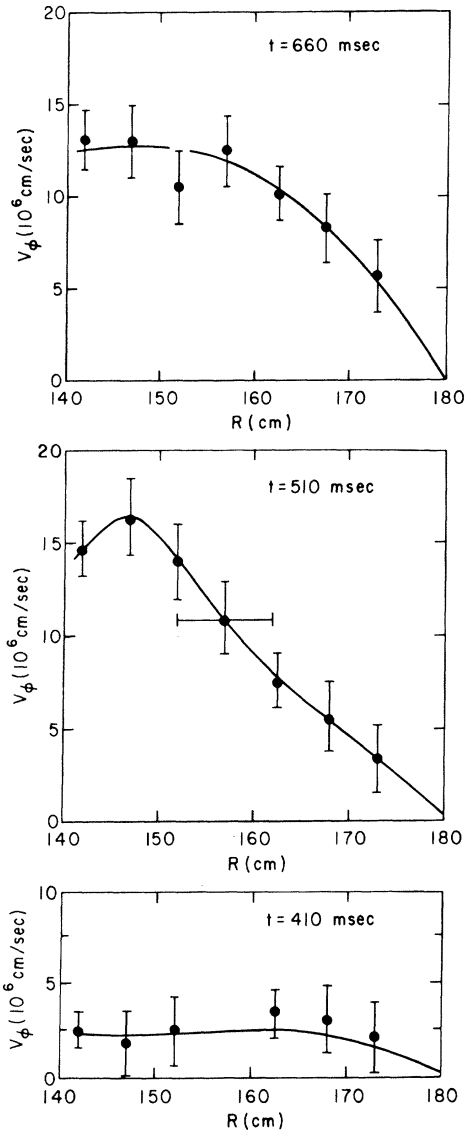

FIG. 24. Toroidal rotation speed radial profiles for the same conditions as in Fig. 23. All values of v_ϕ are measured relative to the value at the plasma edge ($R = 180$ cm).

temperature values at large R, but it can be significantly improved by using a more favorable beam-spectrometer geometry where the spectrometer line of sight crosses the beamline near the sightline tangency point.

The existence of a non-Gaussian line profile arising from the presence of the drifting ion plume was observed during a series of $D^0 \rightarrow He^{2+}$ plasma shots. These were most favorable for such observations because the He^{2+} plasma gives a very high intensity signal while the 21-keV/amu D^0 beams gave a high plume-to-prompt ratio (cf. Fig. 18). Figure 25(a) shows a He II 4686-Å line profile ($R_I = 140$ cm) when the east beam was cut off, and hence the broad component is due to the other neutral beams (including south in Fig. 21) which were on but not viewed directly by the spectrometer. The resulting fit to a double Gaussian profile shows that the wings of the line are poorly modeled, suggesting that radiation from several radii are significantly contributing to the observed emission. The appearance of the highly shifted tail in this figure is probably due more to the fact that the plume intensity is strongest for high-velocity ions which can reach the spectrometer line of sight before being ionized back to He^{2+} than to a very high toroidal rotation speed in the plasma. A detailed analysis of the line profile arising from the ion plume in Fig. 25(a) would involve, among other considerations, a detailed modeling of both the beam profile and parallel ion transport for all radii. Such an effort is beyond the scope of the present work, but we note that these observations serve as an example of the importance of taking ion plume effects into account. A similar result is obtained in this case when only the east beam itself is on, but here the direct charge-exchange signal also contributes and tends to reduce the non-Gaussian component. This is seen in Fig. 25(b), where again the line profile wing is not well matched by the assumed Gaussian profiles. This broad component in the wings of the line when the east beam is off was hardly evident in the $H^0 \rightarrow D^0$ cases plotted in Figs. 23 and 24, reflecting primarily the advantage of using higher energy beams to reduce the relative intensity due to drifting ions and, to a lesser degree, more favorable plasma profiles in these $H^0 \rightarrow D^+$ discharges.

Judicious choice of beam-spectrometer geometry allows

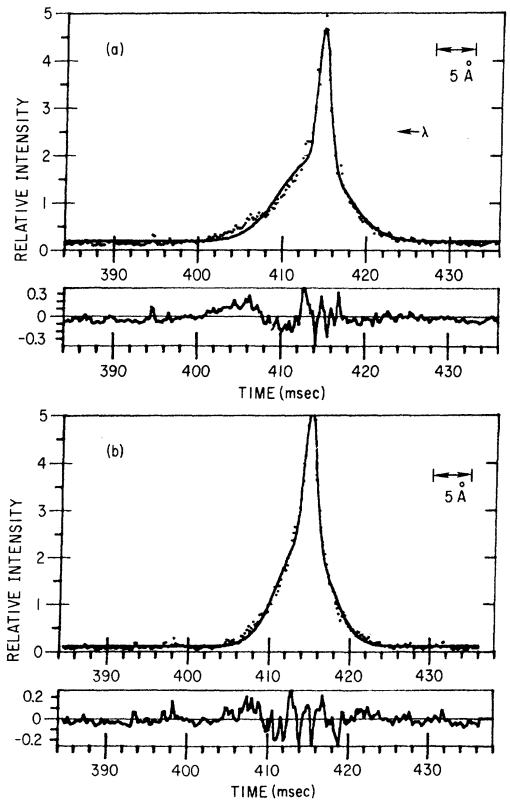

FIG. 25. Non-Gaussian line profiles at 4686 Å due to recombined ions drifting into the spectrometer line of sight. $D^0 \rightarrow He^{2+}$ with geometry as shown in Fig. 21. (a) Line profile with east beam off and south and southwest beams on; (b) line profile with only east beam on. Solid lines are least-squares-fitted Gaussians with fit residuals shown below each line profile.

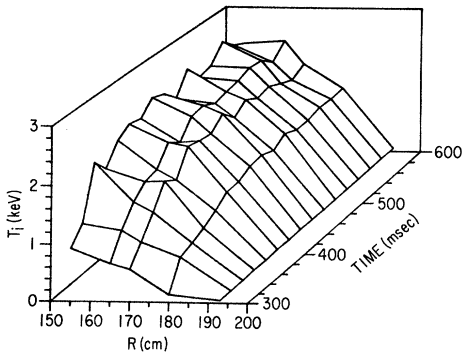

FIG. 26. Time evolution of ion temperature profile for the $D^0 \rightarrow D^+$ case in PDX with the geometry of Fig. 16. Scoop limited discharges with $P_{absorbed} \approx 2.3$ MW, $R_{PI} = 153$ cm, and $a = 40$ cm. Each intersection point on the grid surface represents a datum. The neutral beam was on from 300 to 600 ms.

reasonably accurate $T_i(r,t)$ measurements even with the low-energy D^0 beams. The experimental arrangement on PDX was modified to reflect the arrangement shown in Fig. 16, where the sightline crosses the neutral beam almost at the tangency radius of the sightline. This reduces the radial delocalization due to the ion plume, as indicated in Fig. 20 (the shape of the plume intensity radial distribution is rather insensitive to the neutral beam energy). To reduce any influence from other neutral beams, the northwest beam on PDX was used since this beamline is toroidally separated from all others by at least 80° in either direction. (Modulation of the beam as a means of separating the influence of various beamlines was not available for these experiments.) In addition, an optical multichannel analyzer with an intensified photodiode array (Princeton Applied Research Corporation, Model 1420) was installed to provide spectral line profiles every 20 ms with acceptable signal strength.

A plot of the time evolution of ion temperature radial profiles measured with this system is shown in Fig. 26 for $D^0 \rightarrow D^+$ circular discharges run while testing a particle scoop limiter on PDX.[39] These plasmas were run at densities of $\bar{N}_e \simeq (4\text{—}4.5) \times 10^{13}$ cm^{-3} which resulted in decreasing the He^+ ionization mean free path and hence contributed to decreasing the plume ion intensity, especially from the other beamlines. Reasonable agreement between these results at $r = 0$ ($R_I = 155$ cm) and passive charge exchange was again obtained, and a preliminary analysis of the energy balance for these discharges (using the Princeton Plasma Physics Laboratory TRANSP code[17,40]) indicates that the measured T_i profiles agree to within 20% with those calculated assuming neoclassical ion thermal conductivity. These results are shown mainly to emphasize the wealth of information available using CXRS with just a few plasma shots. A detailed transport and power balance analysis of these discharges using the above results along with other information on the plasma properties will be reported elsewhere.

VI. CONCLUSION

Charge-exchange recombination spectroscopy clearly provides a powerful tool for determining the ion velocity distribution in hot plasmas. Ion temperature profiles can be obtained with good spatial resolution using the relatively benign low-Z impurities that are present in most fusion plasma experiments. With high-beam energies and/or reasonable access for the neutral beam-spectrometer arrangement, simple fiber optically coupled spectrometer systems are feasible, allowing easy access to reactor environments.

The present discussion has considerably expanded our earlier work,[5] and a number of general observations can be made. Plasma effects, especially ion-ion collisions, can mix different l levels and cause substantial changes in expected line intensities. This results in transitions between lower n levels of the hydrogenic ions being the most useful for impurity ion density measurements, and it usually causes a decrease in the intensity of the transitions between higher Rydberg states. In addition, l-mixing effects can raise the expected intensities of background radiation caused by electron impact excitation of the hydrogenic ions.

The effects of apparent line broadening due to atomic fine structure must be evaluated and can change depending on excitation processes. This is especially true when velocity distributions are being studied in detail. For overall ion temperature measurements, a correction to the measured temperature can be applied to obtain the actual ion temperature with a high degree of confidence.

The ions produced by the neutral beam which then drift along magnetic field lines into the spectrometer line of sight and are excited by electron collisions can significantly distort ion temperature and fully stripped ion density measurements. This effect is strongest in very-low-Z elements because of the low charge-exchange cross sections and high electron excitation rates, but may also cause difficulties for interpreting the intensity of $\Delta n = 2\text{-}1$ transitions in the higher-Z elements such as C and O. It is important to recognize that this effect is independent of beam power and cannot be avoided by neutral beam modulation unless the beam modulation time is faster than the transit time of the ions along the field lines. This ion plume intensity can be especially interfering when trying to measure nonthermal ion distributions in He^{2+} or other elements because it can lead to non-Gaussian line profiles due to loss of radial localization of the measurement rather than to any real nonthermal effects.

A very simplified model for calculating the ion plume intensity has been introduced in the foregoing discussion. The use of this one-dimensional model which assumes collisionless ion parallel transport along the field lines, no significant change in the ionization balance due to charge-exchange recombination, and only charge-exchange recombination and electron impact ionization, is not rigorously applicable across the entire plasma cross section. For the case where the ionization path length is greater than the plasma circumference (e.g., for C^{5+} and O^{7+}), the model calculations are best considered to be more estimates than quantitative assessments of the pollution of the prompt charge-exchange signal by excitation of drifting ions. However, it is quite clear from both our simple calculations and our experimental results at low beam energies with unfavorable beam-spectrometer access

that the ion plume intensity has to be considered carefully for each experimental situation. The model used here represents a useful first step for such evaluations.

Ion temperature and plasma bulk motion velocities can be measured in most magnetically confined plasma experiments using CXRS. While not necessary, modulation of the neutral beam power is highly desirable to prevent pollution from other beams and to help discriminate against radiation from the cool plasma edge. Visible spectral lines are most attractive for these measurements due to ease of optical access and spectral analysis, but these are best excited only at higher beam energies. For helium and other very light impurities, a vertical viewing geometry is necessary for the most accurate T_i measurements even though rotation velocity measurements may be sacrificed. If constrained to low energy (<30 keV/amu) neutral beams and a midplane viewing geometry, use of the ultraviolet lines of C^{5+} and O^{7+} will give the most reliable measurements, but fine-structure corrections must be made, especially at low temperatures. This approach is planned for the PBX experiment (a modification of the PDX tokamak).

The goal of reliable and relatively simple time- and space-resolved ion velocity distribution measurements seems readily attainable using CXRS provided attention is paid to the various complications we have discussed. While our discussion has concentrated on ion temperature measurements using He, C, or O in tokamak devices, it is easily expanded to other elements and magnetic confinement geometries. In addition, the considerations of intensities, fine structure, and product ion effects obviously are relevant to other applications of CXRS beyond that of ion temperature and plasma rotation measurements.

ACKNOWLEDGMENTS

The authors wish to thank especially R. Hulse for several seminal suggestions during this work and a critical reading of the manuscript. Useful conversations with D. Post, E. Hinnov, R. Goldston, D. Mueller, H. Kugel, and R. Isler are grateful acknowledged. B. Bransden, R. Olson, T. Green, E. Shipsey, and J. Browne provided us with several preprints of their calculations of theoretical cross sections. Likewise, R. Isler, R. Groebner, and G. A. Cottrell graciously provided us with preprints of their work with CXRS on the ISX-*B*, Doublet-III and DITE tokamaks, respectively. P. Roney helped with much of the necessary software for data acquistion and analysis, and H. Towner provided indispensable aid in the neutral beam attenuation calculations. This work was supported by the U. S. Department of Energy, Contract No. DE-AC02-76-CHO-3073.

[1]Equipe TFR, Nucl. Fusion 18, 647 (1978).
[2]H. Eubank *et al.* in *Plasma Physics and Controlled Nuclear Fusion Research, Proceeding of the 7th International Conference, Innsbruck, 1978* (IAEA, Vienna, 1979), Vol. I, p. 167.
[3]S. Suckewer, H. P. Eubank, R. J. Goldston, J. McEnerney, N. R. Sauthoff, and H. H. Towner, Nucl. Fusion 21, 1301 (1981).
[4]D. E. Post, D. R. Mikkelsen, R. A. Hulse, L. D. Stewart, and J. C. Weisheit, J. Fusion Energy 1, 129 (1981).
[5]R. J. Fonck, R. J. Goldston, R. Kaita, and D. Post, Appl. Phys. Lett. 42, 239 (1983).
[6]R. C. Isler and L. E. Murray, Appl. Phys. Lett. 42, 355 (1983).
[7]R. C. Isler, Phys. Rev. Lett. 38, 1359 (1977).
[8]R. C. Isler, L. E. Murray, S. Kasai, J. L. Dunlop, S. C. Bates, P. H. Edmonds, E. A. Lazarus, C. H. Ma, and M. M. Murakami, Phys. Rev. A 2701 (1981).
[9]A. N. Zimovev, A. A. Korotko, E. R. Krzhizhanovskii, V. V. Afrosimov, and Yu S. Gordeev, Pis'ma Zh. Eksp. Teor. Fiz. 32, 557 (1980) [JETP Lett. 32, 539 (1980)].
[10]R. J. Fonck, M. Finkenthal, R. J. Goldston, D. L. Herndon, R. A. Hulse, R. Kaita, and D. D. Meyerhofer, Phys. Rev. Lett. 49, 737 (1982).
[11]D. E. Post, L. R. Grisham, and R. J. Fonck, Phys. Scr. T3, 135 (1983).
[12]H. Winter, Comm. At. Mol. Phys. 12, 165 (1982).
[13]R. J. Fonck and D. S. Darrow, Bull. Am. Phys. Soc. 28, 939 (1983).
[14]R. C. Isler, R. A. Langley, and L. E. Murray, Bull. Am. Phys. Soc. 28, 941 (1983).
[15]R. Groebner, N. Brooks, K. Burrell, L. Rottler, and P. Thomas, Bull. Am. Phys. Soc. 28, 940 (1983); R. J. Groebner, N. Brooks, K. Burrell, L. Rottler, Appl. Phys. Lett. 43, 920 (1983).
[16]G. A. Cottrell, Nucl. Fusion 23, 1689 (1983).
[17]R. J. Goldston, D. C. McCune, H. H. Towner, S. L. Davis, R. J. Hawryluk, and G. L. Schmidt, J. Comput. Phys. 43, 61 (1981).
[18]R. E. Olson, in *Electronic and Atomic Collisions,* edited by N. Oda and K. Takayunagi (North-Holland, Amsterdam, 1980).
[19]R. E. Olson, Phys. Rev. A 24, 1726 (1981).
[20]T. A. Green, E. J. Shipsey, and J. C. Browne, Phys. Rev. A 25, 1364 (1982).
[21]E. J. Shipsey, T. A. Green, and J. C. Browne, Phys. Rev. A 27, 821 (1983).
[22]H. Ryufuku and T. Watanabe, Phys. Rev. A 18, 2005 (1978).
[23]H. Ryufuku, Japan Atomic Energy Research Institute Report JAERI-82-031, 1982 (unpublished).
[24]M. Rosenbluh, P. Pancok, B. Lax, and T. A. Miller, Phys. Rev. A 18, 1103 (1978).
[25]R. M. Pengelly and M. J. Seaton, MNRAS 127, 165 (1964).
[26]S. O. Kastner, Astron. Astrophys. 54, 255 (1977); S. O. Kastner and A. K. Bhatia, *ibid.* 71, 211 (1979).
[27]V. P. Shevelko, I. Yu. Skobelev, and A. V. Vinogradov, Phys. Sci. 16, 123 (1977).
[28]H. A. Bethe and E. E. Salpeter, *Quantum Mechanics of One- and Two-Electron Atoms* (Plenum, New York 1977), Sec. 17.
[29]H. A. Bethe and E. E. Salpeter, *Quantum Mechanics of One- and Two-Electron Atoms,* Ref. 28, Sec. 55.
[30]N. P. Economou, R. R. Freeman, and P. F. Liao, Phys. Rev. A 18, 2506 (1978).
[31]J. D. Garcia and J. E. Mack, J. Opt. Soc. Am. 55, 654 (1965).
[32]H. G. Kuhn, *Atomic Spectra* (Academic, New York 1969), p. 171.
[33]W. H. M. Clark *et al.*, Nucl. Fusion 22, 333 (1982).
[34]R. Mewe, Astron. Astrophys. 20, 215 (1972).
[35]K. L. Bell, H. B. Gilbody, J. G. Hughes, A. E. Kingston, and F. J. Smith, Culham Laboratory Report CLM-R216 (1981) (unpublished).
[36]F. Wagner *et al.*, Phys. Rev. Lett. 49, 1408 (1982).

[37]S. M. Kaye *et al.*, J. Nucl. Mater. (in press).
[38]S. L. Davis, D. Mueller, and C. J. Keane, Rev. Sci. Instrum. 54, 315 (1983).
[39]R. Budny *et al.*, J. Nucl. Mater. (in press).
[40]R. J. Hawryluk, in Proceedings of the Course on Physics of Plasma Close to Thermonuclear Conditions, Report EUR-FU-RU/XXII/476/80, Vol. I, p. 19.